THE ASTROPHYSICAL JOURNAL, 439:520–541, 1995 February 1

AN ANALYTICAL MODEL FOR THE TRIAXIAL COLLAPSE OF COSMOLOGICAL PERTURBATIONS

DANIEL J. EISENSTEIN[1] AND ABRAHAM LOEB
Astronomy Department, Harvard University, 60 Garden Street, Cambridge, MA 02138
Received 1994 April 26; accepted 1994 August 9

ABSTRACT

We present an analytical model for the nonspherical collapse of overdense regions out of a Gaussian random field of initial cosmological perturbations. The collapsing region is treated as an ellipsoid of constant density, acted upon by the quadrupole tidal shear from the surrounding matter. The dynamics of the ellipsoid is set by the ellipsoid self-gravity and the external quadrupole shear. Both forces are linear in the coordinates and therefore maintain homogeneity of the ellipsoid at all times. The amplitude of the external shear is evolved into the nonlinear regime in thin spherical shells that are allowed to move only radially according to the mass interior to them. The full dynamical equations then reduce to a set of nine second-order ordinary differential equations, which reproduce the linear regime behavior but can be evolved past turnaround, well into the nonlinear regime. We describe how the initial conditions can be drawn in the appropriate correlated way from a random field of initial density perturbations. The model is applied to a restricted set of initial conditions that are more suitable to the above approximations; most notably we focus on the properties of rare high-density peaks ($\gtrsim 2\ \sigma$). By considering many random realizations of the initial conditions, we calculate the distribution of shapes and angular momenta acquired by objects through the coupling of their quadrupole moment to the tidal shear. The average value of the spin parameter, $\langle\lambda\rangle \approx 0.04$, is found to be only weakly dependent on the system mass, the mean cosmological density, or the initial power spectrum of perturbations, in agreement with N-body simulations. For the cold dark matter power spectrum, most objects evolve from a quasi-spherical initial state to a pancake or filament and then to complete virialization. Low-spin objects tend to be more spherical. The evolution history of shapes is primarily induced by the external shear and not by the initial triaxiality of the objects. The statistical distribution of the triaxial shapes of collapsing regions can be used to test cosmological models against galaxy surveys on large scales.

Subject headings: cosmology: theory — large-scale structure of universe

1. INTRODUCTION

In the standard cosmological model, density perturbations grow by gravitational instability from their small initial amplitude to the observed nonlinear structure, thus accounting for the galaxies, clusters, superclusters, filaments, and voids in the present universe (Peebles 1993). Despite the simplicity of these initial conditions, the analytical understanding of the advanced stages of gravitational instability, where the density contrast $\delta\rho/\rho$ exceeds unity, is limited. Numerical codes are frequently used in an attempt to uncover the nonlinear dynamics of collapsing regions and in order to predict the observational consequences of specific models for structure formation. However, simulations are often expensive in computer time and are therefore limited in resolution or total volume. An approximate extension of linear perturbation theory into the nonlinear regime is achieved by the Zel'dovich (1970) approximation (see review by Shandarin & Zel'dovich 1989). Another approach which extrapolates the physics even further, up to the virialization phase of bound objects, is the spherical collapse model (Gunn & Gott 1972; Peebles 1980, § 19). Under the assumption of sphericity, the nonlinear dynamics of a collapsing shell is determined by the mass interior to it and described by the parametric solution to the dynamics of a closed universe. Although the Zel'dovich approximation generically yields pancakes and numerical simulations show that many collapsing regions are filamentary (e.g., Park 1990; Bertschinger & Gelb 1991; Cen & Ostriker 1993), the spherical model became popular because of its simplicity. Most notably, it was integrated into the Press-Schechter formalism (Press & Schechter 1974) for calculating the mass function of collapsed objects in the universe. In reality, overdense regions in galaxy surveys of the local universe (e.g., Geller & Huchra 1989; Maddox et al. 1990; Saunders et al. 1991; Shectman et al. 1992; Strauss et al. 1992) have complicated triaxial shapes with sheets and filaments being common features. Moreover, recent work has demonstrated that the tidal shear plays an important role in the dynamics of collapsing regions (Hoffman 1986b; Dubinski 1992; Bond & Myers 1994; Bertschinger & Jain 1994; van de Weygaert & Babul 1994) and therefore requires a nonspherical analysis. Nonsphericity is also necessary in order to explain the origin of galactic rotation through the coupling of galaxies to tidal torques during their collapse (Hoyle 1949; Peebles 1969; Doroshkevich 1970; Efstathiou & Jones 1979; White 1984; Hoffman 1986a, 1988; Barnes & Efstathiou 1987; Ryden 1988; Quinn & Binney 1992; Warren et al. 1992).

In this paper we construct a new analytical model to study the nonlinear collapse of nonspherical regions in a Gaussian random field of initial density perturbations. The collapsing system is approximated as a triaxial ellipsoid of constant overdensity that is affected by its own gravitational field and by the external tidal shear. The external tidal force can be expanded as a multipole series, with the quadrupole being the dominant relevant term for the internal dynamics of the ellipsoid. Since the quadrupole force and the

[1] Also at Physics Department, Harvard University.

ellipsoid self-gravity are linear functions of the spatial coordinates, they maintain homogeneity of the ellipsoid at all times. The quadrupole shear from the external density field is calculated by dividing the background mass distribution into spherical shells that move only radially. Under these approximations, we reduce the full dynamical equations of motion to a set of second-order ordinary differential equations. The initial conditions can be derived from a Gaussian random field of density perturbations with some power spectrum, and the initial peculiar velocities are chosen to be those of the growing mode. The equations of motion we obtain reproduce the linear regime behavior of the density field. By integrating these differential equations we are able to describe the collapse of a triaxial sheared region into a virialized object. In difference from the spherical approach, the ellipsoid model can be used to study the influence of the external tidal shear on the triaxial collapse of overdense regions. Through many random realizations of the initial density field the model can examine the statistical properties of collapsing systems, including their triaxial shapes, orientation relative to the background density field, and total angular momenta, for different cosmological models.

The outline of this work is as follows. In § 2 we review the equations of motion for a self-gravitating ellipsoid and the approximation (Icke 1973) that allows us to extend this treatment to a homogeneous ellipsoidal overdensity in the universe. We also show that the quadrupole shear can be added to this formulation. In § 3 we present our approximation for the nonlinear evolution of this shear. The restrictions placed upon the initial conditions for the model are described in § 4. Given a Gaussian random field of initial density perturbations, we derive in Appendix A the joint probability distribution for the necessary initial conditions. In Appendix B we describe our treatment of a collapse along a single axis, and in Appendix C we relate the magnitude of the external shear to the amplitude of density fluctuations on a given mass scale in a fashion independent of the initial power spectrum. The statistical properties of collapsing regions are then analyzed in § 5, by applying the above model to many realizations of random initial conditions. Finally, in § 6 we discuss the applications and limitations of the model and indicate potential future work.

2. ELLIPSOID MODEL FOR A COLLAPSING REGION

We begin from a small density perturbation on top of a smooth background assumed to be a Friedmann-Robertson-Walker (FRW) universe. We assume that the background is composed of collisionless cold particles and allow for a nonzero cosmological constant. We pick the origin to be near the center of a region that has a sufficiently high density so that it collapses before its environment. Since we are interested in the properties of the collapsing region, we separate the universe into two disjoint parts, the collapsing high-density region and the rest of the universe. The boundary between these parts is taken to be a sphere centered at the origin. We denote the background density by ρ_b and let the density as a function of space be $\rho(\boldsymbol{x})$, where $\boldsymbol{x}$ is the position vector. We then define $\delta\rho(\boldsymbol{x}) = \rho(\boldsymbol{x}) - \rho_b$ and $\delta(\boldsymbol{x}) = \delta\rho(\boldsymbol{x})/\rho_b$.

The gravitational force exerted on the spherical region by the rest of the universe can be calculated by expanding the external gravitational potential as a multipole series (Binney & Tremaine 1987). Taking the sphere to have radius R, we find

$$\Phi(\boldsymbol{x}) = \sum_{l,m} \frac{4\pi G}{2l+1} a_{lm} Y_{lm} x^l , \tag{1}$$

where $x \equiv |\boldsymbol{x}|$, the Y_{lm} are spherical harmonics, G is Newton's constant, and

$$a_{lm} = \rho_b \int_{|s|>R} d^3s Y^*_{lm} \delta(\boldsymbol{s}) s^{-l-1} . \tag{2}$$

The time-dependent magnitude of the external potential will be calculated in § 3. For now we consider the effect of this potential on the inner region.

We are primarily concerned with the acquisition of angular momentum and the shearing of the inner region. For these purposes, we focus on the quadrupole ($l = 2$) terms. The $l = 0$ term produces no force, and the dipole ($l = 1$) terms produce a uniform acceleration that may move the whole inner region but does not alter the shape or induce any rotation. This motion can indirectly affect the object because the surrounding material will have a new angular distribution relative to the displaced object, requiring a recalculation of the multipole expansion coefficients. However, if the dipole is generated on large scales, then the object and its entire neighborhood move together as a bulk flow and the changes in the angular distribution of matter will be very small, allowing us to ignore the $l = 1$ terms. Previous work has found the quadrupole terms to dominate the higher ($l \geq 3$) terms (Quinn & Binney 1992), and so we ignore all but the $l = 2$ terms.

We model the inner region as a homogeneous ellipsoidal overdensity (Lynden-Bell 1964; Lin, Mestel & Shu 1965; Zel'dovich 1965; Icke 1973; White & Silk 1979). By this, we mean that $\delta(\boldsymbol{x})$ is a constant inside the ellipsoid and zero outside of it. Homogeneous ellipsoids are advantageous because their gravitational potentials depend quadratically on the coordinates and therefore preserve their homogeneity and because they have nonzero quadrupole moments which couple to the $l = 2$ terms of the external potential. Obviously, this approximation ignores all the complexities of shapes and substructure actually present in the central region. However, the object cannot be torqued by its subcomponents, and the time dependence of the quadrupole moments may be well captured by the ellipsoid approximation.

A convenient way to analyze the motion of homogeneous ellipsoids was discussed by Peebles (1980, § 20). The position of the ellipsoid is given by

$$r^\alpha = A^{\alpha\beta} x^\beta , \tag{3}$$

where $\boldsymbol{x}$ is a vector inside the unit sphere and repeated indices are summed. The matrix A is constant in space but depends on time. The mass is evenly distributed over this unit sphere and thus the ellipsoid has a uniform density. If the columns of A are orthogonal, then they are the axes of the ellipsoid, with the lengths of the axes being the magnitude of the respective column. However, since in general the columns of A are not orthogonal, the axes may be found from the relation defining the outer shell of the ellipsoid,

$x^\alpha x^\alpha = 1$. The equation of the ellipsoid is therefore

$$r^T A^{-1T} A^{-1} r = 1 . \tag{4}$$

To rotate to the principal axis frame we diagonalize the matrix AA^T as $Q\Lambda Q^T$, where Q is orthogonal and Λ is real and diagonal because AA^T is symmetric. Then we rewrite equation (4) as

$$(Q^T r)^T \Lambda^{-1} (Q^T r) = 1 . \tag{5}$$

Thus, the axes of the ellipsoid are in the columns of Q and the corresponding axis length is the square root of the corresponding diagonal element of Λ.

Since the gravitational potential of such an ellipsoid may be written as a quadratic function (Peebles 1980), we are prompted to consider a general quadratic potential

$$\Phi(r) = \frac{1}{2} \Phi^{\alpha\beta} r^\alpha r^\beta , \tag{6}$$

where the matrix $\Phi^{\alpha\beta}$ is a function of the matrix A. Then the force per unit mass is just $-\nabla\Phi(r)$, leading to the momentum equation,

$$\frac{d^2 r^\alpha}{dt^2} = -\Phi^{\alpha\beta} r^\beta . \tag{7}$$

By substituting equation (3) in equation (7) we find

$$\frac{d^2 A^{\alpha\beta}}{dt^2} = -\Phi^{\alpha\gamma} A^{\gamma\beta} . \tag{8}$$

This is our basic equation of motion. It is crucial that the potential be quadratic in the coordinates, since this leads to forces that are linear in space. The magnitude of r cancels out, so that all the similar ellipsoidal shells behave in the same way and the ellipsoid remains homogeneous.

We now must construct this quadratic potential. First, we consider the contribution from the ellipsoid. For an isolated ellipsoid of mass M_e, the potential is given by elliptic functions (Peebles 1980) so that,

$$\Phi_{\rm ell}(r') = \frac{1}{2} GM_e[(r'_1)^2 R_D(a_2^2, a_3^2, a_1^2) + (r'_2)^2 R_D(a_1^2, a_3^2, a_2^2) + (r'_3)^2 R_D(a_1^2, a_2^2, a_3^2)] , \tag{9}$$

where a_j are the lengths of the semiaxes and r' is in the principal axis frame. The function R_D is defined as (Carlson 1977; Press et al. 1992),

$$R_D(x, y, z) = \frac{3}{2} \int_0^\infty \frac{dt}{(t + z)\sqrt{(t + x)(t + y)(t + z)}} . \tag{10}$$

Rotating to the original frame by means of $r = Qr'$ yields the matrix

$$\Phi_{\rm ell} = GM_e\{Q \times {\rm diag}\,[R_D(\Lambda^{22}, \Lambda^{33}, \Lambda^{11}), R_D(\Lambda^{11}, \Lambda^{33}, \Lambda^{22}), R_D(\Lambda^{11}, \Lambda^{22}, \Lambda^{33})] \times Q^T\} . \tag{11}$$

Although the potential inside a homogeneous ellipsoid is quadratic, the potential outside is rather complicated. This causes the smooth background outside the ellipsoid to warp, producing a nonquadratic potential inside the ellipsoid and causing it to become inhomogeneous. In order to avoid this problem, we assume that the background remains smooth, with a density equal to that of the unperturbed universe (Icke 1973; White & Silk 1979). The mass of the ellipsoid, including the contribution from the background density in the volume covered by the ellipsoid, is taken to be a constant denoted by M. We then compute the gravitational potential as the sum of two pieces. The first piece comes from the smooth background of density ρ_b, yielding $\Phi_{\rm sph}(r) = 2\pi G\rho_b r^2/3$ and

$$\Phi^{\alpha\beta}_{\rm sph} = \frac{4\pi}{3} G\rho_b I^{\alpha\beta} , \tag{12}$$

where I is the identity matrix. The second piece is associated with the remaining mass of the ellipsoid, and is given by $\Phi_{\rm ell}$ in equation (11) with the mass $M_e \equiv M - \rho_b V$, where $V = 4\pi \det(\Lambda^{1/2})/3$ is the volume of the ellipsoid. This approximation agrees well with N-body simulations (White 1993), because at early times the background is still smooth while at late times the background has a much lower density than the ellipsoid.

The evolution of the background density $\rho_b \propto a^{-3}$ in a matter-dominated universe can be obtained from the FRW equation for the scale factor $a = 1/(1 + z)$,

$$\left(\frac{da}{dt}\right)^2 = \Omega a^{-1} + \Omega_\Lambda a^2 + \Omega_R . \tag{13}$$

We define $\Omega = 8\pi G\rho_b/3H_0^2$, $\Omega_\Lambda = \Lambda_v/3H_0^2$, and $\Omega_R = 1 - \Omega - \Omega_\Lambda$ to quantify the contributions of nonrelativistic matter, the cosmological constant Λ_v, and the space curvature to the expansion of the universe. These quantities are evaluated at the present time, and $H_0 \equiv d(\ln a)/dt|_{a=1}$ is the present Hubble constant.

Next, we note that the $l = 2$ terms of the external shear (eq. [1]) also produce a quadratic potential. Manipulating the spherical harmonics in equation (1) we find

$$\Phi_{\rm shear} = G\sqrt{\frac{\pi}{5}}\begin{pmatrix} 2\sqrt{6}\ {\rm Re}\ a_{22} - 2a_{20} & -2\sqrt{6}\ {\rm Im}\ a_{22} & -2\sqrt{6}\ {\rm Re}\ a_{21} \\ -2\sqrt{6}\ {\rm Im}\ a_{22} & -2\sqrt{6}\ {\rm Re}\ a_{22} - 2a_{20} & 2\sqrt{6}\ {\rm Im}\ a_{21} \\ -2\sqrt{6}\ {\rm Re}\ a_{21} & 2\sqrt{6}\ {\rm Im}\ a_{21} & 4a_{20} \end{pmatrix}. \tag{14}$$

Here the relation $a_{2(-m)} = (-1)^m a_{2m}^*$ was used to eliminate $m < 0$. We choose the real and imaginary parts of a_{22} and a_{21} as well as a_{20}, which is always real, as the five independent real values in the $l = 2$ decomposition. We will discuss the time dependence of the a_{2m} coefficients in § 3 and the issue of how to pick them initially in Appendix A.

With the equation of motion (8) and the potential matrix $\Phi^{\alpha\beta} \equiv (\Phi^{\alpha\beta}_{\rm sph} + \Phi^{\alpha\beta}_{\rm ell} + \Phi^{\alpha\beta}_{\rm shear})$, we may evolve the system of a homogeneous ellipsoid on a smooth background undergoing a time-dependent quadrupole external shear as a set of nine second-order differential equations. For a nonzero cosmological constant, one should also add: $\Phi^{\alpha\beta}_{\rm vac} = -\Lambda_v I^{\alpha\beta}/3$. In order to apply this approach to a collapsing perturbation, we must relate the initial conditions of the ellipsoid and the time dependence of the external shear to properties of the initial density field. As described above, we center the origin of the coordinate systems on a high-density region and construct a sphere about this point to distinguish the collapsing object from its environment. We consider the system at high redshift, so that $\delta \ll 1$. The coefficients a_{2m} that describe the external potential as a function of the initial density field are given in equation (2). We pick the ellipsoid to match the average density, mass, and quadrupole moments of the inner spherical region at the initial time. This choice is independent of initial time to leading order in the linear regime. We define the average overdensity of the inner region at the initial time as

$$\bar{\delta}(R) = \left(\frac{3}{4\pi R^3}\right)\int_{|\boldsymbol{r}|<R} d^3r\, \delta(\boldsymbol{r})\,. \tag{15}$$

The mass of the region is $M = (4\pi/3)\rho_b R^3[1 + \bar{\delta}(R)]$, and the quadrupole moments q_{2m} are defined as

$$q_{2m} = \rho_b \int_{|\boldsymbol{r}|<R} d^3r\, \delta(\boldsymbol{r}) r^2 Y_{2m}^*\,. \tag{16}$$

To match these quantities, we consider an ellipsoid with semiaxes c_1, c_2, and c_3 oriented at some angle relative to the coordinate axes. We pick the overdensity of the ellipsoid to be $\bar{\delta}(R)$. Then the mass of the ellipsoid is $(4\pi/3)\rho_b[1 + \bar{\delta}(R)]c_1 c_2 c_3$ which, when matched to the mass M of the inner region, gives

$$c_1 c_2 c_3 = R^3\,. \tag{17}$$

Finally, the quadrupole moments of the ellipsoidal overdensity are chosen to match those of the actual inner region. First, we label the points of the ellipsoid by $\boldsymbol{r} = QC\boldsymbol{x}$, where $\boldsymbol{x}$ is a point inside the unit sphere, $C = {\rm diag}\,(c_1, c_2, c_3)$, and Q is an orthogonal matrix whose jth column is the direction of the axis with length c_j. We then define the matrix $N = QC^2Q^T$ and note the following integral over the volume of the ellipsoid,

$$\rho_b\bar{\delta}\int_{\rm ellipsoid} d^3r\, r_i r_j = \rho_b\bar{\delta}c_1 c_2 c_3\int_{|\boldsymbol{x}|\le 1} d^3x (Q_{im}C_{mm}x_m)(Q_{jn}C_{nn}x_n) = \rho_b\bar{\delta}R^3\left(\frac{4\pi\delta_{mn}}{15}\right)Q_{im}C_{mm}Q_{jn}C_{nn} = \frac{M_e}{5}N_{ij}\,, \tag{18}$$

where $M_e = (4\pi/3)\rho_b\bar{\delta}(R)R^3$ is the mass of the ellipsoid above the background. Now we may find the q_{2m} of the ellipsoid in terms of the matrix N; for example,

$${\rm Re}\ q_{22} = \rho_b\bar{\delta}\int_{\rm ellipsoid} d^3r\sqrt{\frac{15}{32\pi}}(r_1^2 - r_2^2) = M_e\sqrt{\frac{3}{160\pi}}(N_{11} - N_{22})\,. \tag{19}$$

These relations may be inverted, so that given all the q_{2m} we find N to be

$$N = \sqrt{\frac{40\pi}{3}}\frac{1}{M_e}\begin{pmatrix} {\rm Re}\ q_{22} - \dfrac{1}{\sqrt{6}}q_{20} & -{\rm Im}\ q_{22} & -{\rm Re}\ q_{21} \\ -{\rm Im}\ q_{22} & -{\rm Re}\ q_{22} - \dfrac{1}{\sqrt{6}}q_{20} & {\rm Im}\ q_{21} \\ -{\rm Re}\ q_{21} & {\rm Im}\ q_{21} & \dfrac{2}{\sqrt{6}}q_{20} \end{pmatrix} + \tau I\,, \tag{20}$$

where the constant τ in front of the identity matrix is unknown. We then diagonalize N to find Q and C^2, the latter depending on τ, and impose the condition in equation (17) to determine τ. With this condition we find the lengths and directions of the axes of the ellipsoid. We then set the initial value of A to be QC.

Since the equation of motion is second-order, one must specify the initial velocities. We pick the velocities so that the density field is a pure growing mode, consistent with the fact that we normalize the power spectrum today when only the growing mode had

survived. In linear theory the peculiar velocities are given by (Peebles 1980, § 14)

$$\delta v = \frac{2fg}{3H\Omega}, \tag{21}$$

where g is the peculiar gravitational acceleration, H is Hubble's constant, and $\Omega = \rho_b/\rho_c$ is the cosmological density parameter. Here $f = (a/D)(dD/da) \approx \Omega^{0.6}$, a is the expansion factor of the universe, and D is the linear growth factor. Since $g = -\Phi r = -\Phi A x$, the initial velocity field is

$$v = \frac{dA}{dt}\, x = Hr - \frac{2f}{3H\Omega}\,\Phi r, \tag{22}$$

and so we find

$$\frac{dA^{\alpha\beta}}{dt} = HA^{\alpha\beta} - \frac{2f}{3H\Omega}\,\Phi^{\alpha\gamma}A^{\gamma\beta}. \tag{23}$$

In this way we have related the initial conditions of the equation of motion to $\bar{\delta}$ and the five q_{2m}.

After evolving the ellipsoid through the matrix A, we wish to measure properties of the ellipsoid, such as its angular momentum and energy. The axes of the ellipsoid are the eigenvectors of AA^T and the lengths of the semiaxes are the square roots of the eigenvalues. Labeling these lengths as c_j, the potential energy of the ellipsoid is given by (Binney & Tremaine 1987)

$$W = -\frac{3}{5}\,GM^2 \int_0^\infty \frac{d\tau}{\sqrt{(\tau + c_1^2)(\tau + c_2^2)(\tau + c_3^2)}}. \tag{24}$$

Here we have neglected the potential energy from the background density and from the tidal shear, both of which are small at late times when this quantity is of interest and when $M_e \approx M$. The kinetic energy equals (Peebles 1980, § 20)

$$T = \frac{1}{2}\,\rho_e \int v^2\, d^3r = \frac{\rho_e \det A}{2} \int_{|x|<1} \frac{dA^{ik}}{dt}\,\frac{dA^{jk}}{dt}\, x^i x^j = \frac{M}{10}\,\mathrm{tr}\left(\frac{dA}{dt}\,\frac{dA^T}{dt}\right), \tag{25}$$

where ρ_e is the ellipsoid density. The total energy is $E = T + W$. Next, the jth component of the angular momentum is

$$L_j = \rho_e \int (r \times v)_j\, d^3r = \rho_e \det A \int_{|x|<1} \epsilon^{jkm} A^{kn}\,\frac{dA^{mp}}{dt}\, x^n x^p = \frac{M}{5}\,\epsilon^{jkm}\,\frac{dA^{mn}}{dt}\,A^{kn}, \tag{26}$$

where ϵ^{jkm} is the Levi-Civita antisymmetric tensor. The mass of the ellipsoid M is constant, and at late times the contribution from the smooth background is small. With these definitions we can construct the spin parameter λ that measures the amount of rigid rotation acquired by the ellipsoid before virialization,

$$\lambda \equiv \frac{L\sqrt{|E|}}{GM^{5/2}}. \tag{27}$$

3. TIME DEPENDENCE OF THE EXTERNAL SHEAR

In the equation of motion (8) for the ellipsoid, one must specify the time dependence of the external shear. The model described in § 2 considers only quadrupole tidal forces and therefore requires a limited amount of information about the mass distribution outside the ellipsoid boundary. In this section, we will try to develop a simple model for the time dependence of the a_{2m} coefficients.

The simplest approach is to treat the entire volume outside the spherical boundary of the inner region by linear perturbation theory. The motivation for this approach is that because the inner region is a high-density peak, it is likely to be the first object in its neighborhood to collapse. Other high peaks are sufficiently far away that their collapse does not substantially change the tidal force, since such collapses do not move matter on large angular scales as seen from the origin. If the tidal field is determined by scales much larger than the inner region, the evolution of the quadrupole moments would be well treated by linear theory.

In linear theory, the fractional overdensity $\delta(x)$ scales by a uniform growth factor $D(t)$ when considered in comoving coordinates (Peebles 1980). From equation (2), we have

$$a_{2m} = \rho_b \int_{|s|>R} d^3s\, Y^*_{2m}\delta(s)s^{-3}, \tag{28}$$

where the s coordinates are in physical (nonexpanding) space. Rescaling to comoving coordinates, however, makes no difference because the magnitude of s appears equally in the numerator and denominator. The density ρ_b scales as $(1 + z)^3$, where z is redshift. Thus in linear theory,

$$a_{2m}(t) = a_{2m}(t_i)\,\frac{D(t)}{D(t_i)}\left(\frac{1 + z[t]}{1 + z[t_i]}\right)^3, \tag{29}$$

where t_i is the time when we pick the initial conditions. In a flat matter-dominated universe, $D \propto (1 + z)^{-1}$ and $a_{2m} \propto (1 + z)^2$.

The time dependence given in equation (29) can be substituted into the equation of motion for the ellipsoid. When this is done and an ensemble of random ellipsoid realizations are integrated until full collapse, we find the average value of the spin parameter λ to be smaller than 0.01. Since N-body simulations typically find $\langle\lambda\rangle \approx 0.05$ (Barnes & Efstathiou 1987; Warren et al. 1992), the linear approach apparently underestimates the external torque. It is not surprising that the external shear cannot be purely described by linear theory, since the material just outside the boundary of the object has a density similar to that of the object. As the ellipsoid collapses, the nearest shell surrounding it follows its infall. Since the contribution of a mass element to a_{2m} depends on the inverse cube of its distance from the origin, the fact that material near the object tends to be closer than its initial comoving position means that it should produce more torque than linear theory predicts.

Based on the fact that the material around the peak tends to be closer than linear theory predicts, we divide the external mass distribution into N spherical shells, all centered on the origin, and evolve each shell according to the mass interior to it (Gunn & Gott 1972). Each shell carries a fraction of the quadrupole shear, initially determined from the Gaussian random field, and this shear is scaled according to the radial collapse of the shell. The essential aproximation is that we neglect the tangential redistribution of the matter within shells. This approximation is justified so long as the motion of the matter subtends a small angle, as viewed from the origin, which is always true for matter at large radius. Using growing mode velocities, we need to specify only the average overdensity interior to the shell $\bar{\delta}$ in order to determine its motion.

To calculate the time dependence of the shear in this approximation, we first note that a_{2m} depends on $\delta\rho(x)$ but not on rescaling of the radial coordinate. We find $\delta\rho$ by solving the spherical evolution from some initial overdensity $\bar{\delta}(t_i)$ using the FRW equation (13),

$$\frac{d^2r}{dt^2} = -\frac{4\pi G\rho_i}{3r^2} + \frac{\Lambda_v r}{3}, \tag{30}$$

with initial density $\rho_i = (1 + \bar{\delta})\rho_b(t_i)$ and $r(t_i) = 1$. The initial velocity is to leading order $H(t_i)(1 - \bar{\delta}/3)$, with

$$H(t_i) = H_0\sqrt{\Omega(1 + z_i)^3 + \Omega_R(1 + z_i)^2 + \Omega_\Lambda}, \tag{31}$$

where z_i is the redshift at the initial time t_i. Thus for a given $\bar{\delta}$, we may integrate equation (30) to find $r(t)$. We then find $a_{2m}(t) \propto \delta\rho$ by considering the difference between the top-hat density, $\rho_{\rm sph} \propto r^{-3}$, and the background density, $\rho_b \propto (1 + z)^3$. Thus,

$$\frac{a_{2m}(t)}{a_{2m}(t_i)} = \frac{(1 + \bar{\delta}_i)r(t)^{-3} - \{[1 + z(t)]/[1 + z_i]\}^3}{\bar{\delta}_i}. \tag{32}$$

For a sufficiently early initial time in the matter-dominated epoch, $\bar{\delta}_i \ll 1$ and $\Omega \approx 1$, so that equation (32) matches the linear theory result of $a_{2m} \propto (1 + z)^2$.

To implement this approach, we wish to consider N shells, with radial boundaries R_α, for $\alpha = 0, 1, \ldots, N$. We take R_0 to be the radius of the spherical boundary that separates the ellipsoid region from the external region and $R_N = \infty$ to indicate that the outer shell includes everything outside the outermost spherical shell. Initially each shell carries a fraction of the quadrupole shear

$$a_{2m}^{(n)} = \rho_b \int_{R_{n-1}<|s|<R_n} d^3s\, Y_{2m}^*\, \delta(s) s^{-3}, \tag{33}$$

where $n = 1, 2, \ldots, N$ labels the shell. We pick the characteristic overdensity of each shell as

$$\bar{\delta}^{(n)} \equiv \frac{1}{2}\left(\bar{\delta}[R_{n-1}] + \bar{\delta}[R_n]\right). \tag{34}$$

For thin shells the differences between the definitions $\bar{\delta}^{(n)}$ and $\bar{\delta}(R_n)$ defined in equation (15) is small. The overdensity surrounding the outermost shell R_{N-1} is negligible, so we set $\bar{\delta}^{(N)} = 0$ and treat the tide of the outermost shell using linear theory.

The above model for the exterior region completes the necessary set of equations and allows us to evolve the ellipsoid beyond the linear regime according to equation (8). This approach requires a large set of initial data: the overdensities $\bar{\delta}$ for all the shells and for the inner region, the quadrupole shears a_{2m}^α for all outer shells, and the quadrupole moments q_{2m} for the inner region. This set comprises $6N + 5$ real numbers, randomly drawn in a highly correlated way from a Gaussian random field of initial density perturbations. By treating the random density field in spherical coordinates, as suggested by Binney & Quinn (1991), we can separate this set of random numbers into six independent sets, each of which is distributed as a multidimensional Gaussian distribution. We describe how to find these distributions in Appendix A. We may then draw the initial conditions from the proper probability distribution by taking linear combinations of $6N + 5$ random Gaussian deviates.

4. COLLAPSE AND CONSTRAINTS

If the ellipsoid is simply evolved forward in time, one soon reaches the obvious problem that the axes collapse at different times. Typically, one axis turns shorter and collapses first, forming a pancake (Lin et al. 1965; Zel'dovich 1970; Peebles 1980) in which the baryons shock and the dark matter goes through violent relaxation. The computation of angular momentum should not end at the time of the short axis collapse, since the other two axes are still extended and give the object a significant quadrupole moment with which it couples to the tidal shear. Previous work on spherical objects (Ryden 1988) has shown that most of the angular momentum is acquired near turnaround, since most of the time is spent at this phase. In the ellipsoid model, turnaround is not a single epoch and it appears necessary to follow the system as long as the quadrupole moments are large, i.e., until the long axis turns around. After the short axis collapses, it makes a small contribution to the quadrupole moment of the ellipsoid. The quadrupoles are

proportional to the difference between the squares of the axis lengths and so the exact dynamics of the virialization process along the short axis has little effect on the acquisition of angular momentum.

We therefore follow the approximation of Bond & Myers (1994) and impose a strict cutoff on the collapse of an axis, namely that no axis may collapse below 40% of its maximum length. This keeps the dynamics from approaching the singularity at zero length and simulates the virialization of the corresponding axis. The 40% cutoff was picked to allow the ellipsoid to be slightly flatter than the spherical virial theorem would predict, but because the collapsed axis is much shorter than the noncollapsed ones, the exact cutoff value does not affect the angular momentum acquisition significantly. The implementation of this constraint is nontrivial because the ellipsoid may be rotating and the columns of the matrix A are in general not orthogonal. The details of this implementation are presented in Appendix B. Note that the vorticity of the ellipsoid is conserved under the equation of motion (8), but is not conserved through this treatment of the collapse of an axis. Also, since the kinetic energy of the ellipsoid is being altered, energy is not conserved. Because the change in the total energy during the dynamics is usually small, we save the last value of the energy before the first axis collapses and use it in the calculation of the spin parameter λ.

In principle, we would like to evolve the ellipsoid until all three axes collapse, by which time the angular momentum gained by tidal torques (i.e., not by accretion) will be complete. The first difficulty is that in some cases one or two axes do not collapse at all. The existence of a high-density region does not guarantee that it will not be sheared by its environment to form a wide pancake. This would be true even if we were to use linear theory for the shear, as can be seen from the Zel'dovich approximation (Zel'dovich 1970). In this approximation, if a volume element begins with an outward peculiar velocity along one of its axes, then it will continue to move outward for all later times. Because the region is overdense, all the growing mode velocities resulting from the ellipsoidal perturbation will be inward. But since the trace of $\Phi_{\rm shear}$ is zero at least one eigenvalue of $\Phi_{\rm shear}$ is negative, and therefore in at least one direction, the peculiar velocity will be less inward than for the isolated ellipsoid. We wish to study regions that end as spatially bounded objects. In $\Omega = 1$ cosmologies, following the Zel'dovich approximation, we require that the radial component of the initial peculiar velocities inward in all directions. This corresponds to requiring that the potential matrix be positive definite. In $\Omega < 1$ cosmologies, however, this condition is not sufficient because mildly overdense regions may still expand forever. Only regions which exceed the critical density collapse, so we instead require that the inward radial component of the peculiar velocities exceed that of the growing mode of a spherical top-hat perturbation at the critical density, which corresponds to an initial overdensity

$$\bar{\delta}_{\rm crit} = \frac{3}{5}\left[\frac{\Omega_R}{\Omega}(1+z_i)^{-1} + \frac{\Omega_\Lambda}{\Omega}(1+z_i)^{-3}\right]. \tag{35}$$

Due to nonlinear effects of the external shear, our requirement is not a perfect discriminator as to whether an axis will expand forever, but it at least matches the weakly nonlinear theory. The consequences of this constraint are examined analytically in Appendix C.

Since we base the time dependence of the shear on the density of the spherical shell collapse, the shear force diverges as the shell collapses to a zero radius. Because the average overdensity of the innermost shell is not so different from that of the ellipsoid, the two objects collapse at similar times. But in most cases, the action of the shear causes the long axis to collapse significantly later than the inner external shell. We must end the integration at some time before the collapse of the inner tidal shell. We therefore choose to end at the time at which a sphere whose overdensity was that of the initial ellipsoid would collapse to a zero radius. We then constrain the initial conditions so that none of the exterior shells has an overdensity $\bar{\delta}^{(n)}$ greater than 95% of the initial density of the ellipsoid. This ensures that the external tidal shells do not collapse before the integration ends. This condition has the important property of tending to make the inner region a density peak; we do not explicitly require that it is truly a peak, but if the overdensity as a function of radius is forced to drop as one moves away from the central region, only extreme variations as a function of angle would allow the density to rise radially in a particular direction.

The last and most significant constraint we impose is that the inner region must have a high overdensity. This condition underlines the separation between the collapsing region and the rest of the universe. We implement this constraint by requiring $\bar{\delta}(R_0) > \nu_{\rm min}\sigma$, where $\nu_{\rm min} = {\rm const}$ and σ is the rms amplitude of mass fluctuations $\delta M/M$ for such regions. As usual, the latter is calculated to be (Bardeen et al. 1986)

$$\sigma^2 = \frac{1}{2\pi^2}\int_0^\infty dk\, P(k)\left[\frac{3j_1(kR_0)}{R_0}\right]^2, \tag{36}$$

where $P(k)$ is the power spectrum and j_1 is a spherical Bessel function. In § 5 we will typically pick $\nu_{\rm min} \gtrsim 2$, thus forcing the central region to be rare.

The above three constraints—(i) $\bar{\delta}(R_0) > \nu_{\rm min}\sigma$; (ii) the overdensity of the surrounding shells being less than 95% of $\bar{\delta}(R_0)$; and (iii) all peculiar velocities being inward—are not implemented directly into the probability distributions for the initial conditions as derived in Appendix A. Rather, we generate sets of the initial conditions and then reject cases that do not satisfy these constraints. Since the strictest condition is $\bar{\delta}(R_0) > \nu_{\rm min}\sigma$, we set up the probability distribution so that $\bar{\delta}(R_0)$ depends on only one Gaussian deviate, which allows us to reject a set of initial conditions on the basis of one random number. Then we can choose the overdensity of the innermost shell to depend on only one more deviate, allowing another straightforward test.

We call the fraction of sets of initial data that meet the above conditions the acceptance rate A. Prior to imposing these constraints, the Gaussian random field was unconstrained. Because the central region is at a mass scale $M = (4\pi/3)R_0^3$, the number density of such regions is $n_0 = \rho_0/M$, where ρ_0 is the mass density today of nonrelativistic matter (i.e., the matter making up the ellipsoid). This means that after applying the constraints, the number density of accepted regions is An_0. If we now construct an ensemble of such regions and, after evolving each of them with our model, find that a given property occurs in some fraction f of them, then the actual number density of such objects is predicted to be fAn_0. We apply this approach elsewhere to predict the

number density of black hole progenitors formed in the initial collapse of objects with very low values of angular momentum (Eisenstein & Loeb 1995, hereafter Paper II).

This completes the description of our model. We next study the statistical properties of collapsing regions in specific cosmological models, defined by the values of the cosmological parameters: Ω, Λ_v, and H_0, as well as by the power spectrum of primordial density perturbations. For a given mass scale, we consider many realizations of the random initial conditions, evolve each realization separately, and then combine the results to analyze the statistical distribution of shapes and angular momenta of collapsing regions.

5. RESULTS

To illustrate the behavior of the model, we adopt a cold dark matter (CDM) power spectrum (Bardeen et al. 1986) of initial density perturbations for two different universes: a flat universe with $\Omega = 1$, and an open universe with $\Omega = 0.2$; both cases assuming $\Lambda_v = 0$ and $H_0 = 50$ km s^{-1} Mpc^{-1}. We normalize the power spectrum by choosing the present rms amplitude of mass fluctuations within an $8h^{-1}$ Mpc radius sphere to be $1/b$, where b is the bias parameter. We pick the initial time to correspond to redshift $z_i = 1000$, and then scale the power spectrum using the growth factor $D(t_0)/D(t_i)$.

The parameters of the model are the mass of the central region M, the minimum peak height $\nu_{\rm min}$, and the radii of the external shells. We consider a variety of mass scales between 10^8 and 10^{15} $M_\odot$. As peak thresholds we use both $\nu_{\rm min} = 2.5$ and 2.0. The radius of the innermost spherical boundary R_0 is fixed to match the mass scale being studied, and we pick all other radii to be multiples of this inner radius. We choose 20 shells, with boundaries at 1, 1.5, 1.75, 2, 2.5, 3, 3.5, 4, 4.5, 5, 6, 7, 8, 9, 10, 12, 15,17, 20, and 30 times the inner radius, as well as at infinity. The only important number in this list is the first one, which implied that the innermost shell is thick. This is done in order to keep the acceptance rate reasonable, as the overdensity of the closest outer shell must be less than 95% of that of the inner region. Were this shell to be thin, the overdensity constraint would only rarely be satisfied. The finite thickness of this shell ultimately limits the radial resolution of the external shear profile.

We consider the flat universe with $b = 1$ for a variety of mass scales and for $\nu_{\rm min} = 2.5$. The average value of λ increases slightly with mass, from 0.034 at 10^8 $M_\odot$ to 0.038 at 10^{12} $M_\odot$ and to 0.049 at 10^{15} $M_\odot$. Figure 1 shows the probability distribution of the spin parameter $P(\lambda)$ for the mass scales of 10^{12} $M_\odot$ and 10^{15} $M_\odot$ in a flat universe. The histograms are based on samples of random realizations that result in 2×10^5 accepted systems for each mass scale. The weak dependence of the mean values of $\langle\lambda\rangle$ on the mass scale is in good agreement with N-body simulations (Barnes & Efstathiou 1987; Warren et al. 1992).

The primary reason for the actual dependence of $\langle\lambda\rangle$ on M is the shape of the power spectrum. With the CDM power spectrum, higher mass scales have larger average quadrupole moments (relative to σMR^2). This results in more elongated initial ellipsoids and therefore in stronger couplings to the external torque. In addition, the fixed choice of shell boundary radii introduces a systematic mass dependence because the higher mass systems have a steeper density profile and a larger fraction of the shear carried by the inner shells (these two profiles are related, as shown in Appendix C). Consequently, the effective shell resolution appears coarser for high-mass objects. The limited resolution results in a slight underestimate of the shear at late times, when the shear amplitude is large.

For $\nu_{\rm min} = 2.5$ only a fraction 0.00621 of all regions satisfy the constraint $\bar{\delta}(R_0) > \nu_{\rm min}\sigma$. The remaining two constraints (shell densities and inward velocities) are satisfied 64.2% of the time for 10^8 $M_\odot$ and 89.7% for 10^{12} $M_\odot$. Most of these additional rejections are due to the inner shell having too high an overdensity; rejections due to the peculiar velocities not being inward occur in less than 3% of the cases (cf. Appendix C). With peak threshold values of $\nu_{\rm min} = 2.5$ and 2.0, the average values of ν are 2.84 and 2.40, respectively, independent of mass scale.

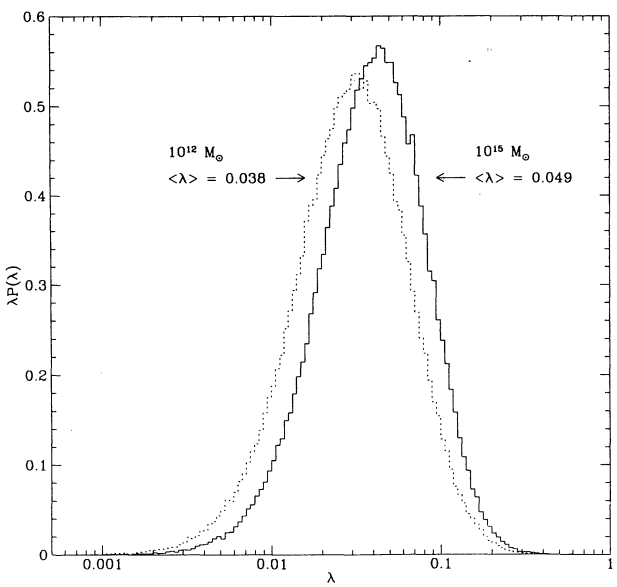

FIG. 1.—Probability distribution of the spin parameter $P(\lambda)$ for the mass scales of 10^{15} $M_\odot$ and 10^{12} $M_\odot$ and $\nu_{\rm min} = 2.5$ in an $\Omega = 1$ universe. Each histogram includes 2×10^5 random realizations of the initial conditions. The average values $\langle\lambda\rangle = \int_0^\infty \lambda P(\lambda) d\lambda$ are also shown.

For a flat universe, the model is strictly independent of the bias parameter or the Hubble constant. Both parameters rescale space and time without altering the collapse dynamics. This does not hold in an open universe, where an intrinsic timescale appears at the transition point to an open curvature-dominated expansion of the background.

The value of λ is found to be anticorrelated with $\nu = \bar{\delta}/\sigma$, so that higher peaks tend to have lower angular momentum (see also Hoffman 1986a, 1988). The linear correlation between the two is about 0.21. Therfore, the choice of $\nu_{\rm min}$ affects the distribution of λ. For a flat universe and $M = 10^{12}\,M_\odot$ we find $\langle\lambda\rangle = 0.038$ for $\nu_{\rm min} = 2.5$ and $\langle\lambda\rangle = 0.051$ for $\nu_{\rm min} = 2.0$. For $10^{15}\,M_\odot$ we find $\langle\lambda\rangle = 0.049$ for $\nu_{\rm min} = 2.5$ and $\langle\lambda\rangle = 0.069$ for $\nu_{\rm min} = 2.0$. If we use a particular ν for all iterations, as opposed to the usual requirement of $\nu > \nu_{\rm min}$, then for $10^{15}\,M_\odot$ we find $\langle\lambda\rangle = 0.089$ for $\nu = 2$, $\langle\lambda\rangle = 0.060$ for $\nu = 2.5$, and $\langle\lambda\rangle = 0.042$ for $\nu = 3$.

In all of the accepted objects, the shortest axis reaches collapse by the end of the integration (i.e., by the time a spherical perturbation with the same initial density as the ellipsoid would have reached zero radius). For $\nu > \nu_{\rm min} = 2.5$, the middle axis reaches collapse in 78% of all iterations, while the long axis reaches turnaround in 84% of the iterations and reaches full collapse in 1.5% of all cases. If we force $\nu = 2$, the corresponding numbers are 65%, 58%, and 0.6% respectively for $M = 10^{12}\,M_\odot$, with a weak dependence on mass. The failure of the long axis to collapse is expected; since it is being pulled out by the shear, it collapses later than the unperturbed spherical case. The few times that the long axis happens to collapse result from the small window of opportunity between the sphere reaching 40% of its turnaround radius (defined as axis collapse) and reaching a zero radius. The failure to turnaround usually is the result of the shear leaving one axis with only a tiny inward velocity so that it undergoes a very long excursion, but it can also result from extreme cases where the rapidly increasing shear toward the end of the integration causes one axis to expand again after it had already been contracting. The dependence of the amount of collapse on ν reflects the tendency of the shear to pull lower peaks apart. Although we require that the velocities are initially inward, this may not be sufficient to guarantee that the object remains bounded under the influence of the nonlinear shear. As suggested in Appendix C, the constraint to have inward velocities is almost negligible for $\nu > 2.5$, with acceptances over 97%, but is important for $\nu = 2$, where the acceptance drops to 82%. The drop means that more systems have one axis with a nearly zero peculiar velocity; these axes are very slow to turnaround. Low-ν systems therefore have larger axis ratios resulting in larger couplings to the quadrupole torques. The correlation between the peak height ν and the axis ratios leads to the above dependence of λ on ν.

Let us now turn to discuss the axis ratios of the evolving ellipsoids. Figures 2–8 present the axis ratios b/a and c/a for various ensembles of ellipsoids. The semiaxis lengths a, b, and c are ordered so that $a \geq b \geq c$. Panels (a)–(e) show the ensemble at different times, while panel (f) shows the mean of the points in the previous panels.

Figure 2 presents the evolution of the axis ratios for a random ensemble of $10^{15}\,M_\odot$ ellipsoids with $\nu = 2$ in the $\Omega = 1$ cosmology. We chose to fix ν rather than use a threshold value $\nu_{\rm min}$ so that the integration of each ellipsoid would end at the same time. The time

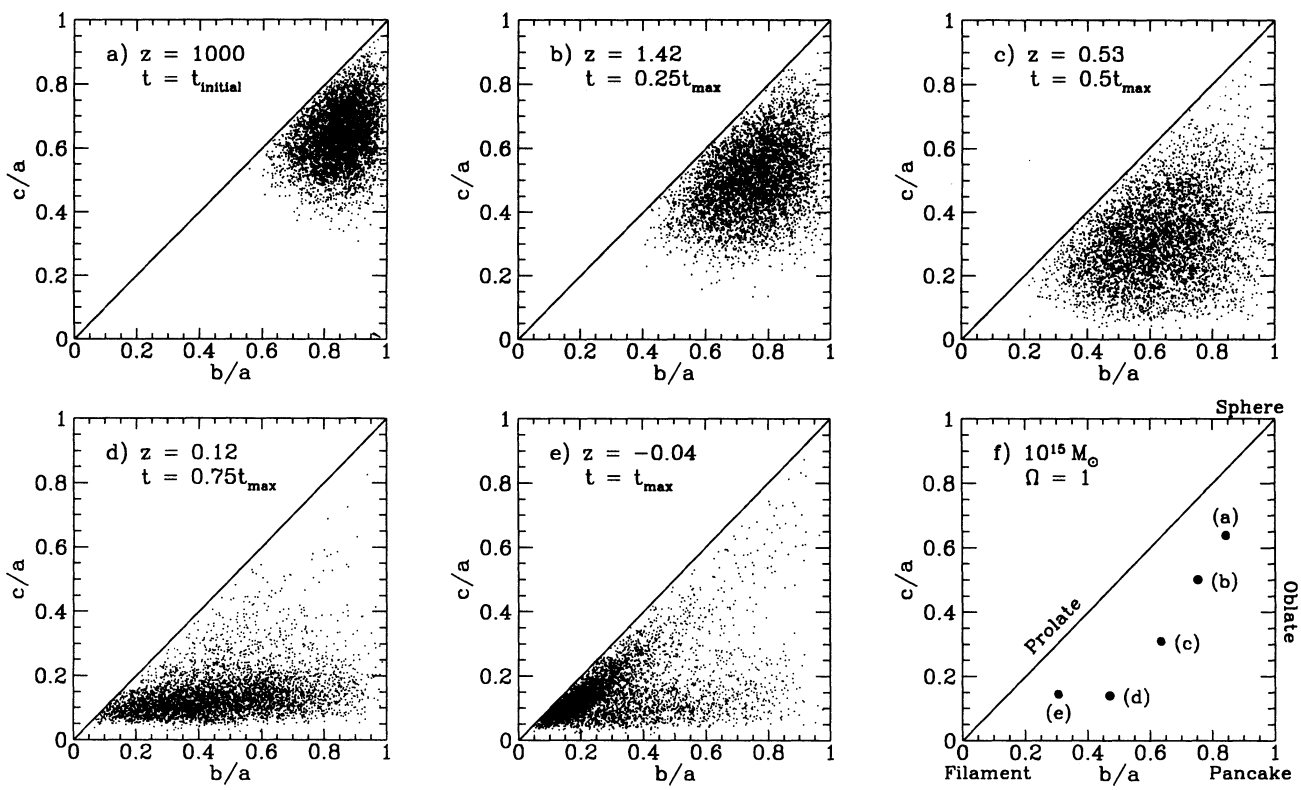

FIG. 2.—Distribution of axis ratios for an ensemble of 5000 systems of mass $10^{15}\,M_\odot$ and $\nu = 2$ in an $\Omega = 1$ universe. (a) Initial distribution; (b)–(d) resulting evolution at particular times. (e) Distribution at time $t_{\rm max}$, the end time of the integration defined by the collapse time of a homogeneous spherical perturbation with the same initial density as the ellipsoids. (f) Mean values of the distributions in the other panels. We define the axis lengths as $a \geq b \geq c$. To find the redshifts we assumed a bias parameter of 1.3 and $H_0 = 50\ {\rm km\ s^{-1}\ Mpc^{-1}}$.

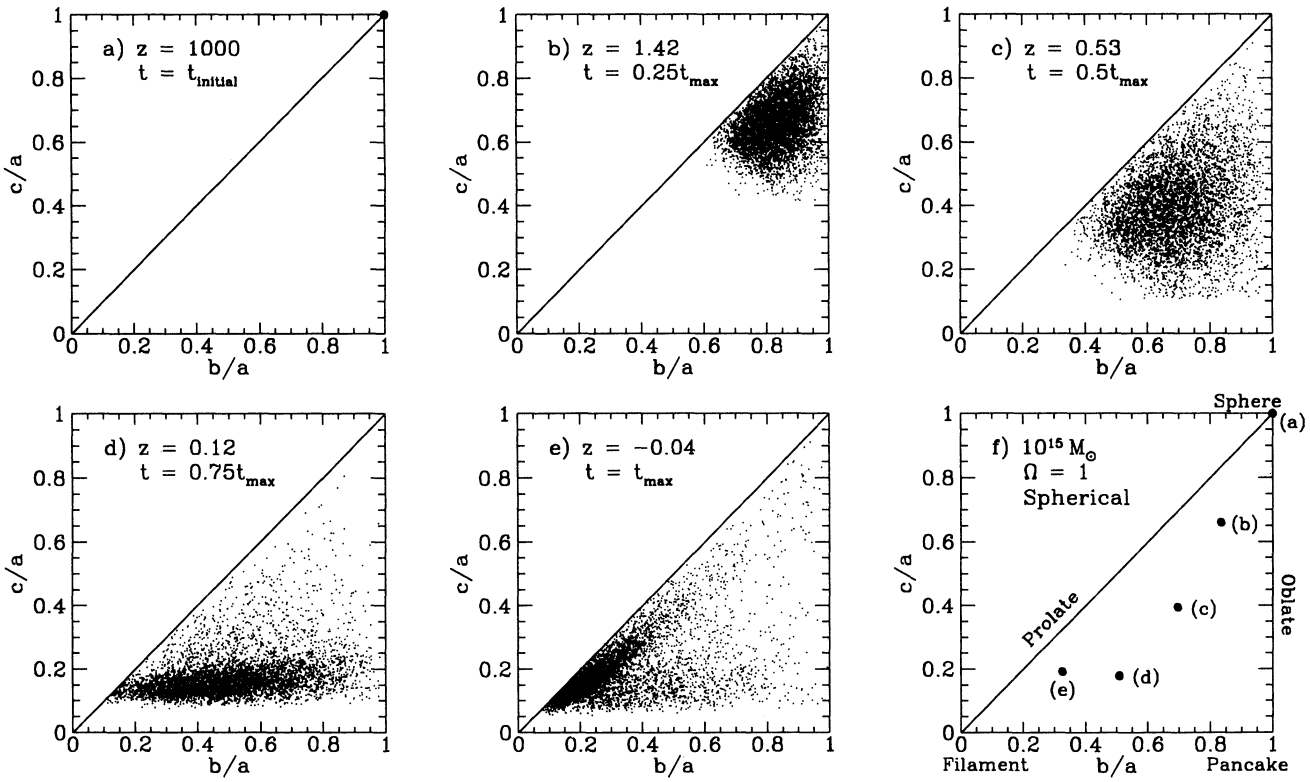

FIG. 3.—As in Fig. 2, but with the initial ellipsoid replaced by a sphere of the same density. The external shear was unchanged.

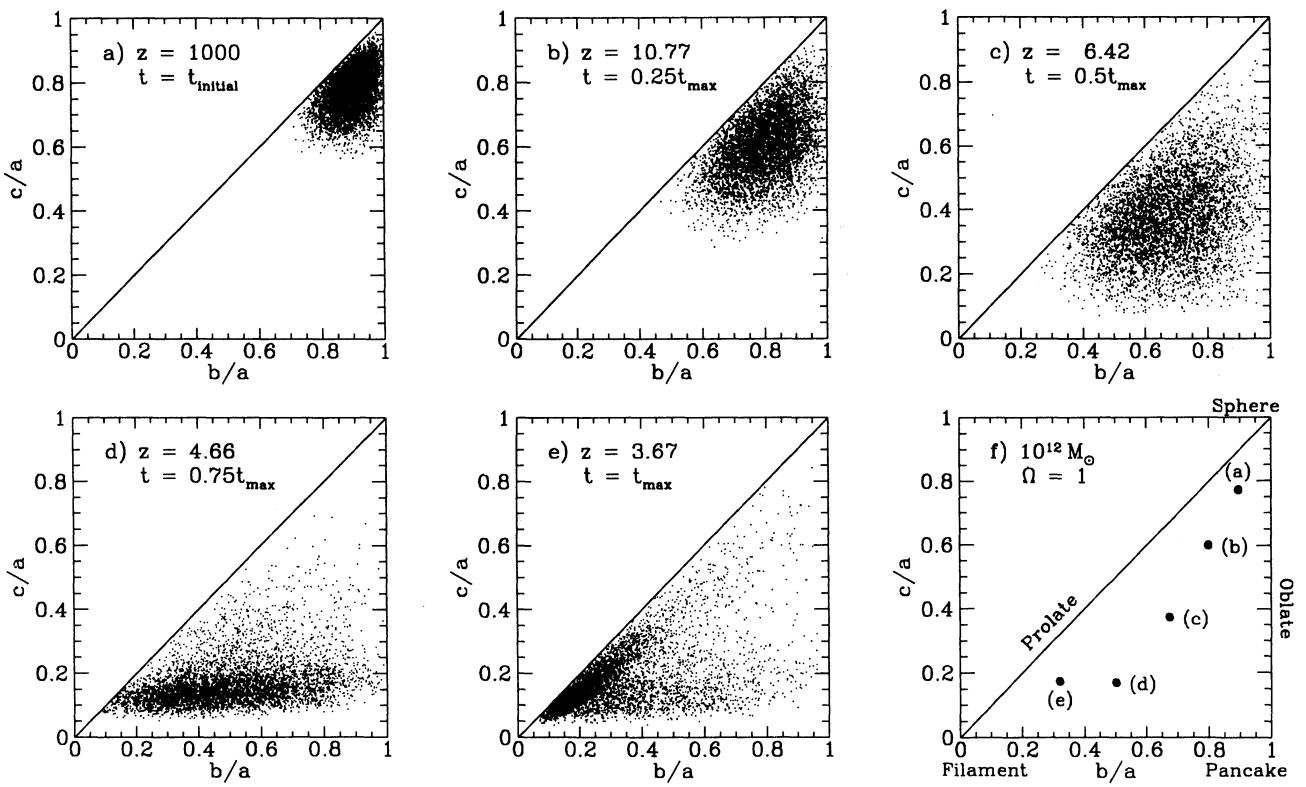

FIG. 4.—As in Fig. 2, but for $10^{12}\ M_{\odot}$ regions

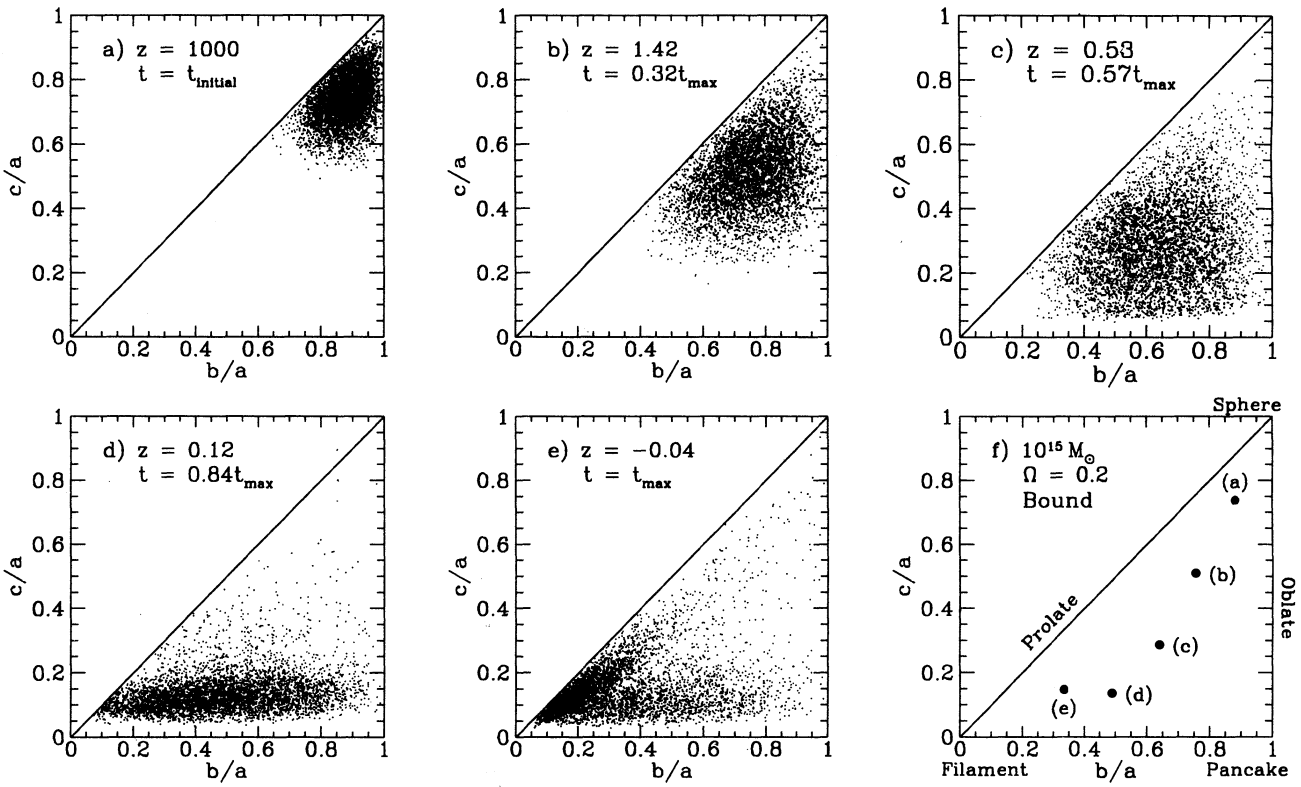

FIG. 5.—As in Fig. 2, but for an open universe with $\Omega = 0.2$, $H_0 = 50$ km s^{-1} Mpc^{-1}, and no bias ($b = 1.0$). For 10^{15} $M_\odot$ ellipsoids, we pick $\nu = 2.2$ in order to match the final collapse redshift of Fig. 2 and then pick the time slices to match the other redshifts of that figure.

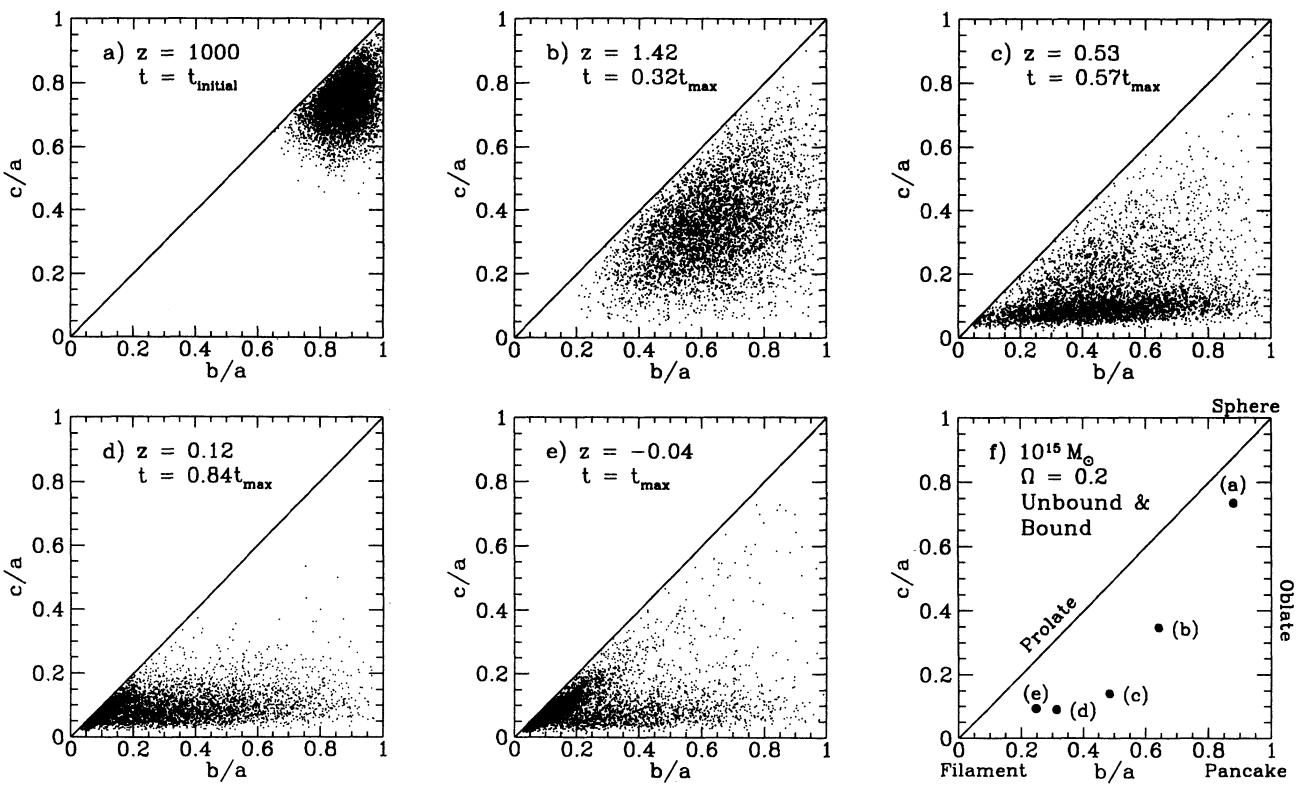

FIG. 6.—As in Fig. 5, but after removing the constraint on the initial peculiar velocities. This allows the inclusion of objects with at least one axis that is likely to expand without bound.

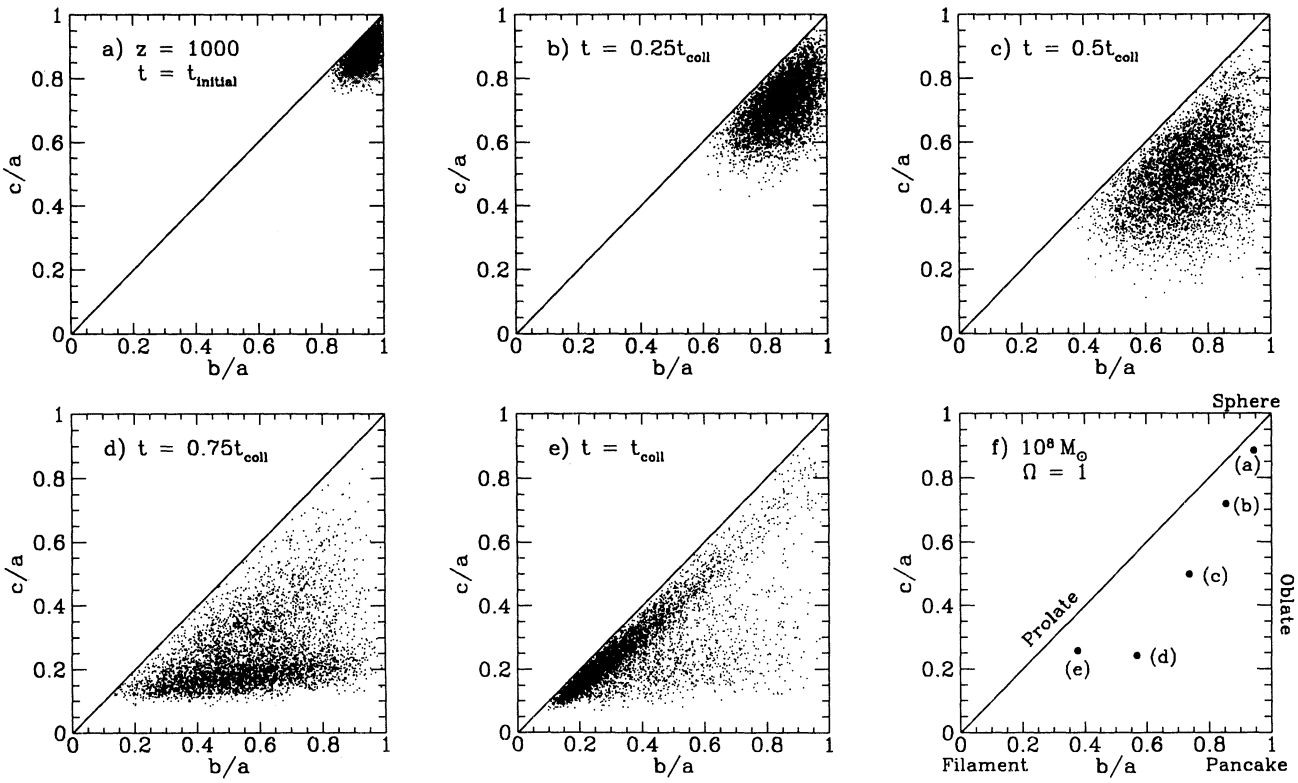

FIG. 7.—As in Fig. 2, but for $10^8\ M_\odot$ regions

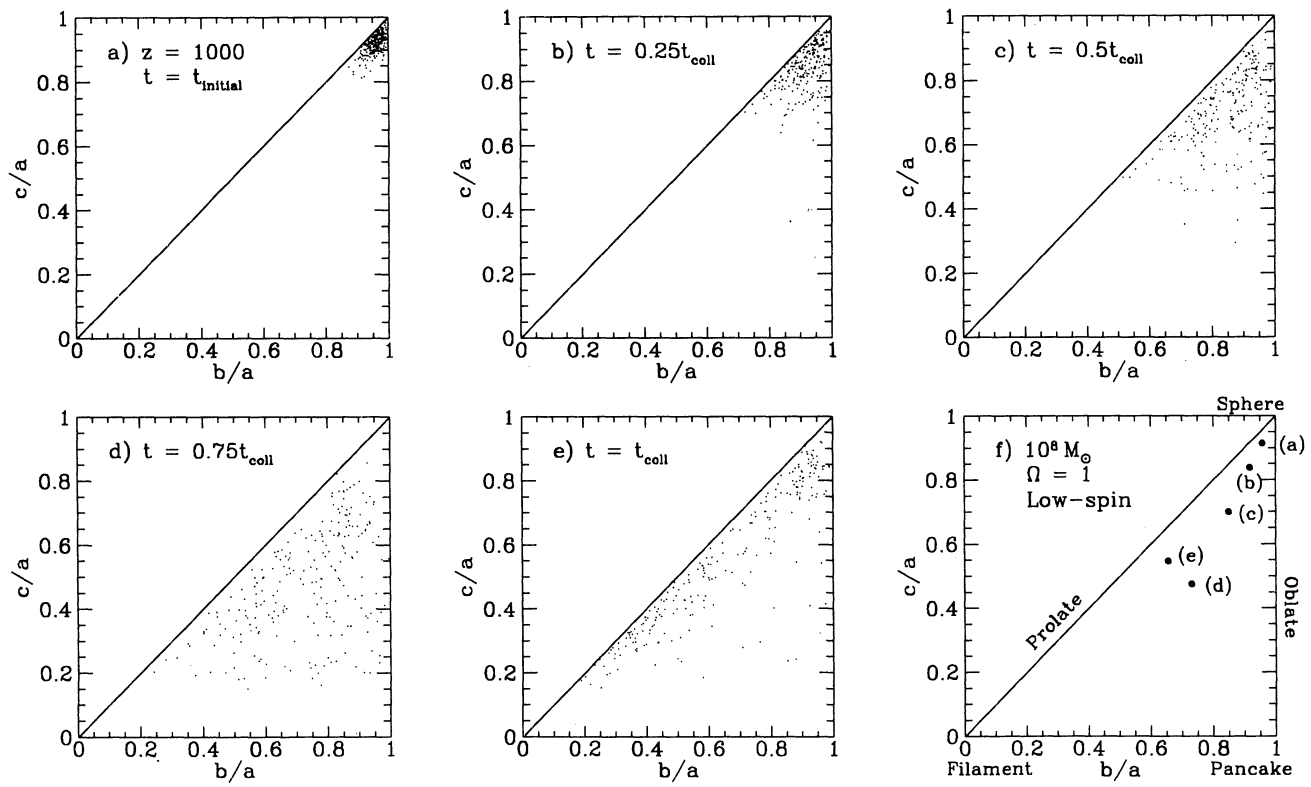

FIG. 8.—As in Fig. 7, but showing only the 232 low-spin objects from an overall sample of 2×10^5 systems

slices in the plots show each ellipsoid at a constant fraction of the collapse time t_{max} for a spherical top-hat perturbation of the same initial density. We track 5000 ellipsoids and show that axis ratios at the initial time and 25%, 50%, 75%, and 100% of t_{max}. We set $b = 1.3$ so that the end time is close to $z = 0$.

The most significant aspect of this plot is the progression of the points from a quasi-spherical initial state to a prolate end state. At early times (panels [*a*]–[*c*]) the short axis falls behind in the expansion so that the points move down the plot. At the time of panel (*d*) the short axis has generally collapsed; however, the typical resulting shape is not an oblate pancake or a prolate filament but rather triaxial. As the evolution continues the middle axis turns around and collapses, so that most objects become prolate by the end time in panel (*e*). Note the slight regeneration of high c/a points between panels (*d*) and (*e*); this corresponds to the beginning of a collapse along the long axis. Indeed, 37 of these 5000 ellipsoids reached long-axis collapse (i.e., the long axis reached 40% of its maximum length).

In contrast to previous discussions on collapsing ellipsoids (Lin et al. 1965; Zel'dovich 1965; Icke 1973; White & Silk 1979), we find that the collapsing region geometry is primarily determined by the external shear and not by the initial anisotropy of the ellipsoids. To demonstrate this result, we alter the model and replace the initial ellipsoid by a sphere. The results for a mass of 10^{15} $M_\odot$, $\Omega = 1$, and $\nu = 2$, are shown in Figure 3. The evolution is very similar to Figure 2 despite the qualitative change in the initial conditions, although the ratio of the long axis to the short axis is not quite as large at late times. Furthermore, even in the full ellipsoid model, the direction of the long axis is dominated by the direction of the shear rather than the direction of the long axis of the initial ellipsoid. This is particularly the case for low mass scales and for higher ν, where the initial quadrupoles are weak and the initial conditions are closer to the spherical example. Even an initially spherical object can gain angular momentum because the shear direction changes as the relative weighting of the shells evolves with time. The resulting value of λ is lower for the spherical case, however, indicating that the anisotropy of the initial ellipsoid is important for the acquisition of angular momentum. For the parameters in this paragraph, $\langle\lambda\rangle = 0.089$ when the initial object is the usual ellipsoid, but $\langle\lambda\rangle = 0.028$ when the initial object is changed to a sphere.

In Figure 4, we consider the mass scale of 10^{12} $M_\odot$ and $\nu = 2$ in the $\Omega = 1$ cosmology (the redshifts assume $b = 1.3$). Compared to Figure 2, the initial ellipsoids are more spherical and have weaker quadrupole moments. However, the axis ratios at late times are similar to those at the 10^{15} $M_\odot$ mass scale.

We next consider the open cosmology with $\Omega = 0.2$ and $b = 1$. For the 10^{15} $M_\odot$ mass scale we pick $\nu = 2.2$ so that the final redshift of the calculation matches that of the flat universe case. The results are presented in Figure 5. Here we have chosen the time slices so that the redshifts are the same as in Figure 2. The slices are no longer evenly spaced in time because of the different cosmology. Due to changes in the power spectrum, the objects are initially more spherical in an open universe, but they end with very similar axis ratios to those obtained in a flat cosmology.

A major difference between the open and the flat cases is that the constraint on the initial velocities is far more severe in the open cosmology. In the open case we require that the peculiar velocities not only be inward but that they be larger in magnitude than those induced by a critically bound sphere. For the above open cosmology and the above mass scale this condition (cf. eq. [35]) requires that a spherical top-hat perturbation have $\nu > 1.1$. Including the disruptive effects of shear (cf. Appendix C), we find that the acceptance rate for this constraint drops down to 23% from its value of 83% for $\Omega = 1$. Thus most $\nu = 2$ peaks have one axis that is not critically bound. In Figure 6, we relax the constraint on the velocities entirely so as to investigate how the general peak behaves in this open universe. There are two notable differences between this plot and either Figure 5 or Figure 2. First, the collapse of the shortest axis, as shown by the accumulation of the points near the horizontal axis, occurs in panel (*c*) rather than in panel (*d*). The relaxation of the velocity constraint allows larger shears to enter. This not only tends to pull out the long axis but also tends to push in the short axis, since the shear is a traceless matrix. The short axis in this sample therefore collapses faster. Second, at the final time in panel (*e*), the objects are significantly more filamentary (note that small deviations in the plotted ratio c/a near zero correspond to large changes in the filament shape a/c). This effect occurs because the long axis expands without bound and the short axis collapses earlier than before. Comparing Figures 2 and 6, we see that when viewed at equal redshifts, open universes have significantly more filamentary structure than flat universes. This occurs primarily because of the stronger influence of shear on the collapsing regions.

Next, we consider the low-spin tail of the population of collapsing regions (cf. Fig. 1). Because of its low angular momentum, the gaseous component of the systems in this tail can collapse to small radii and form compact massive objects. The low-spin systems therefore provide environments that may favor the formation of seeds for quasar black holes; we discuss this possibility in detail in Paper II. For the present discussion, let us examine the qualitative properties of low-spin systems selected out of a population of collapsing regions with $\nu_{min} = 2.5$ on the mass scale of 10^8 $M_\odot$ in a flat universe (including the velocity constraint as usual). Figure 7 shows the full distribution of the ensemble of runs for this mass scale. The different panels show the ellipsoid axis ratios at fixed fractions of the collapse time t_{max} of a spherical perturbation with the same initial density as the ellipsoid. Since ν is not constant, the collapse time is different for different ellipsoids. Thus, the panels in the figure are not equal time slices, but instead show each ellipsoid relative to a measure of timescale for its development.

We now compare this full distribution to the distribution of the subset of low-spin systems. For the definition of a low-spin system, we use the criterion developed in Paper II to determine whether the gas in a system can settle into a sufficiently compact disk with a viscous timescale shorter than the star formation time $\sim 10^7$ yr (i.e., $y < 1.1 \times 10^{-3}$ in the notation of Paper II). This condition translates to a maximum value for the angular momentum per unit mass of the system, $J/M = 8.6 \times 10^{24}$ cm^2 s^{-1}. Since this threshold involves only the total angular momentum, it does not precisely correspond to a bound on the spin-parameter λ (which depends on the energy as well); nevertheless, it is approximately the condition $\lambda \lesssim 10^{-3}$. In a set of 2×10^5 accepted systems, 232 satisfy this limit. In Figure 8, we plot the axis ratio histories of these objects. Evidently, these objects evolve in a much more spherical way than the typical cases shown in Figure 7; over half of the low-spin systems have axis ratios between 2:1 and 1:1 at the end time. This striking result is a consequence of two correlated effects. First, the low-spin systems have closer to spherical initial conditions, but second and more important, the quadrupole shear in their neighborhood is weak. One should also consider the

existence of a background population of accidental low-spin objects. Because of the time dependence of the shear, it is possible for the angular momentum of a filamentary object to be rapidly changing at late times and by chance be small at the end of the integration. Such elongated objects are obviously not environments that would favor black hole formation. While some of these background objects do occur, Figure 8 demonstrates that most of the low-spin events are indeed close to spherical during their evolution.

We close this section by showing four individual cases for the collapse of a $10^{15}\ M_\odot$ object in an $\Omega = 1$ universe with $b = 1.3$. Figures 9*a* and 9*b* show two objects with $\nu = 2$, while Figures 9*c* and 9*d* show two objects with $\nu = 3$. In all cases, the first panel shows the semiaxis lengths as a function of time (note the different timescales between the two values of ν). The freezing of the axis length after its collapse (cf. Appendix B) is evident. The second panel shows the evolution of the overdensity $\delta\rho/\rho = \bar{\delta}$ for the ellipsoid (*solid line*), as well as for the spherical perturbation with the same initial density (*dotted*) and for the Zel'dovich approximation when applied to the initial quadratic potential (*dashed*). The slope discontinuities in the ellipsoid density are a result of halting the collapse of the axes; if this treatment was avoided the ellipsoid would have reached an infinite density slightly before its spherical counterpart. The Zel'dovich approximation does well at early times but underestimates the density after turnaround. The third panel shows the spin parameter as a function of time. While λ grows roughly linearly with time, there are significant secondary variations which are more pronounced at lower mass scales. The four different figures are shown to illustrate a variety of collapse conditions. Figure 9*a* ends with relatively large values of λ and the axis ratios. Figure 9*b* was picked because of the unusual wiggle in its evolution; such wiggles result from a time-varying shear and are not uncommon in the $\nu = 2$ systems when the overdensity is not high enough to dominate the shear. Figure 9*c* is a typical high-ν object; its λ and axis ratios are close to the mean. Finally, Figure 9*d* has a relatively low λ but a large ratio of its long-to-short axes.

6. DISCUSSION AND CONCLUSIONS

In this work we have developed a model for the nonlinear collapse of a triaxial overdense region out of a Gaussian random field of primordial density perturbations. The model approximates the collapsing region as a homogeneous ellipsoid. We assume that the collapsing mass originates in a spherical volume around a high-density peak[2] and select an ellipsoid that matches the mass, mean overdensity, and quadrupole moment of the initial overdensity field in this volume. This choice is independent of redshift to leading order in linear perturbation theory. The mass distribution outside the sphere exerts a tidal torque on the ellipsoid and spins it up. We calculate the quadrupole moment of the external shear as a function of time by dividing the background density field into thin spherical shells that move only radially according to the mass interior to them. The dynamics of the ellipsoid is determined by its self-gravity and the external shear through a set of nine ordinary differential equations. Both forces are linear in the coordinates and therefore maintain homogeneity of the ellipsoid at all times. In Appendix A we have developed the formalism necessary to randomly determine the initial conditions for this model in the appropriate correlated way from a Gaussian random field of initial density perturbations.

The above model was applied to a restricted set of initial conditions that are more suitable to its assumptions. In particular, we studied the statistical properties of rare high-density peaks with a mean overdensity $\bar{\delta} \gtrsim 2\ \sigma$. In a bottom-up hierarchy of structure formation, most objects evolve from a quasi-spherical initial state to a pancake or a filament and then to complete virialization. As demonstrated by Figure 3 (where the initial conditions are spherical), this evolution history of shapes is primarily induced by the tidal shear and not by the initial triaxiality of the ellipsoids. Thus, *the existence of sheets and filaments in the universe is not a result of the Lin-Mestel-Shu (1965) instability*, but rather an environmental effect; namely, the ellipsoids are being sheared by nearby mass concentrations. As shown in Figures 2 and 6, the redshift evolution of the triaxiality of systems on a given mass scale can be used to discriminate between an open and a flat universe. However, the average value of the spin parameter (cf. Fig. 1) $\langle\lambda\rangle \approx 0.04$, is found to be only weakly dependent on the object mass or the cosmological parameters, in agreement with N-body simulations. There is a modest dependence of λ on the peak height ν.

The ellipsoid model incorporates significant qualitative improvements over previous analytical investigations of λ. Other models (Ryden 1988; Quinn & Binney 1992) considered spherical dynamics for the collapsing region and assumed zero initial peculiar velocities rather than growing mode velocities. The latter assumption causes a significant overestimate of λ since it makes the object expand to a larger radius. Quinn & Binney (1992) considered the dipole term of the external potential to be most important, but they worked in the instantaneous rest frame of the center of mass rather than in the actual accelerating rest frame of the center of mass. This led to a nonzero torque even in a uniform gravitational field. In this work, we have ignored the dipole term because the uniform gravitational field that it produces can only cause the object to move linearly and cannot directly induce any rotation. However, this can still affect the dynamics indirectly, since the motion of the object relative to its exterior causes the angular distribution of the exterior matter to change. This would require a recalculation of the multipole moments a_{lm} of the exterior potential at each time step. We avoid this complicated procedure by assuming that the dipole field is predominantly generated at large scales. Therefore, both the object and its immediate neighborhood feel the same force and move together, allowing the change in the angular distribution of the torquing material to be small. To test this assumption quantitatively, we consider the rms value of the dipole field generated outside a sphere of radius R as a function of R. Using the methods of Appendix A, we find that $\langle a_{1m}(R)\rangle_{\rm rms} \propto \{\int_0^\infty dk P(k)[j_0(kR)]^2\}^{1/2}$, where $P(k)$ is the power spectrum and j_0 is a spherical Bessel function. Then, for the standard CDM power spectrum we find that the dipole is indeed generated at large scales, with 96% of the field coming from mass scales bigger than $10^{12}\ M_\odot$ and 50% coming from mass scales bigger than $8 \times 10^{15}\ M_\odot$. Thus, especially on small mass scales, the neglect of dipole terms seems justified.

[2] As shown in Appendix C, only high-density peaks are likely to survive as bound systems under the influence of the external tidal shear from their environment. This effect provides another reason for associating virialized objects, like galaxies or clusters, with high-density peaks.

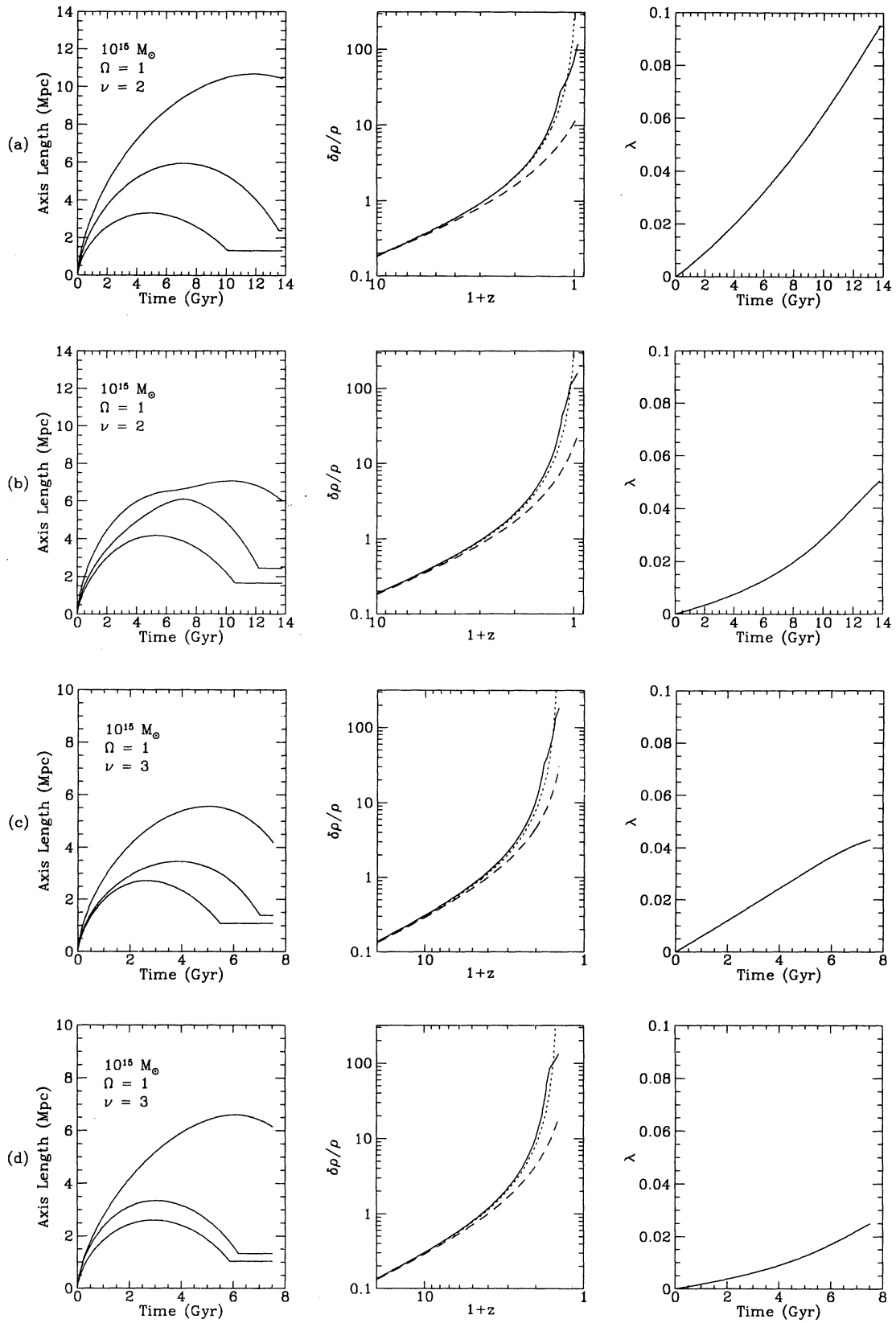

FIG. 9.—Four individual examples of ellipsoids evolved by the model (panel sets [*a*]–[*d*]). Left panel of each set shows the lengths of the three semiaxes as functions of time. Middle panel of each set shows the overdensity of the ellipsoid (*solid line*) as a function of redshift z. Also shown are the overdensity of a spherical top-hat perturbation of equal initial density (*dotted line*) and the overdensity predicted from applying the Zel'dovich approximation to the initial potential (*dashed line*). Right panel shows the spin parameter λ as a function of time.

One limitation of the ellipsoid model is that a homogeneous ellipsoid cannot represent the substructure of the object, as described by the multipole expansion of its mass distribution beyond the monopole and quadrupole terms. This means that we cannot treat such interesting complexities as the distributions of matter and angular momentum within the collapsing object. We have instead focused on global properties of the object, such as its shape and total angular momentum. The dominance of the quadrupole torque over higher moments in linear theory (Quinn & Binney 1992) suggests that our global treatment of the angular momentum is sound.

In assessing the applicability of our model, we return to the initial ellipsoid. The matter inside this ellipsoid makes up the final object. The ellipsoid is picked to match the mean overdensity and quadrupole moment of the inner spherical region. As it traces the density, one may consider the boundary of the ellipsoid as an approximation to the smoothed isodensity contour of the inner region. The model then follows the evolution of this contour and would therefore be useful for applications where the final object is indeed associated with the initial high-density contours.

A potential example for such an application is the collapse of clusters of galaxies. Clusters correspond to high-density peaks on the $10^{14-15}\ M_\odot$ mass scale. In the bottom-up hierarchy of structure formation, the galaxies that inhabit the cluster form before the cluster collapses. Since galaxies tend to form in high-density regions, the high-density environment of the cluster peak favors galaxy formation. Galaxies therefore tend to trace the smoothed density field near the top of the peak, and the ellipsoid model could describe their motion during the formation of the cluster. Obviously the model cannot describe the final virialization process of clusters, where violent relaxation erases in part the signature of the initial conditions. The ellipsoid model predicts however that the outer unvirialized parts of clusters which are still infalling today would be highly triaxial with the axes ratio distribution as shown in Figures 2 and 5. This prediction can be tested by observations of the galaxy distribution around clusters or by deep X-ray imaging of their surrounding gas distribution. In fact, the Virgo Cluster is observed to be elongated considerably along the line of sight based on Tully-Fisher distances (Fukugita, Okamura, & Yasuda 1993). The existence of prolate systems allows for a systematic contamination of optical samples of rich clusters by cases of a chance alignment between a prolate filament and the line of sight. Similarly, clusters that are elongated perpendicular to the line of sight may not have been identified as clusters when examined by spherical filters (e.g., Abell 1958). In addition, prolate clusters introduce a systematic bias into the Sunyaev-Zel'dovich (SZ) effect by favoring low values of the Hubble constant when the data analysis is done using a spherical model for the cluster. Indeed, attempts to determine the Hubble constant from SZ measurements tend to get relatively low values of H_0, occasionally below the permitted lower bound of 50 km s^{-1} Mpc^{-1} (McHardy et al. 1990; Birkinshaw & Hughes 1994, and references therein). Conversely, when the value of the Hubble constant is eventually determined by other techniques, it would be possible to get constraints on the triaxiality of clusters from their SZ effect.

In some other applications, the final object evolves from a region that has little to do with the density contours near the top of a high-density peak. For example, the matter that forms a galactic halo may come from regions of low initial overdensity near the peak. These low-density regions can be assembled into the halo not only by the gravitational attraction of the peak itself but also by the external shear. Initially, the total densities of the "low" and "high" density regions are similar because the background density dominates in both cases. The actual boundary of a virialized object today is an equal collapse-time surface that maps into a complicated surface in the initial density field according to the intervening action of the external shear. To illustrate this complicated situation, consider a high-overdensity region acted upon by a quadrupole tidal shear. The initial region has a slightly anisotropic shape, but this is quickly counteracted by the shear (cf. Figs. 2 and 3). The density contours are pulled into a strongly triaxial shape, as one axis is pushed in by the shear and a second axis is pulled out; the third axis is somewhere in between. As the central peak collapses along its short axis, which is more likely to be considered as part of the object: the high-density regions located far out on the long axis or the lower density regions located nearby on the short axis? For the formation of a galactic halo, the nearby regions are more relevant, since they are positioned closer to the center of mass and therefore undergo shell crossing earlier. Moreover, the sections of the high initial density contours out on the long axis are susceptible to being separated from the halo by fragmentation or other instabilities (Merritt & Hernquist 1991). Thus, the initial isodensity contours around the peak may not be appropriate tracers of the volume that eventually makes up the halo.

An additional problem is that while a galaxy corresponds to the region surrounding a high-density peak, the peak itself collapses at high redshifts and the surrounding matter accretes onto this seed. Hence, the properties of the collapsed peak do not reflect the properties of the final halo. In a spherical collapse model, one hopes to remedy this problem by picking the radius of the object so that the overdensity inside that radius corresponds to a collapse at present. However, when the effects of shear and nonsphericity are included, this procedure is no longer valid.

For the above reasons, we feel that the ellipsoid model does not provide a fully satisfactory description of the dynamics of typical galactic halos. However, the model does substantially better in describing low-spin objects at high redshifts (cf. Paper II). Such objects are generally located in regions with low shear, so that their collapse is more spherical, as demonstrated in Figure 8. This fact tends to reduce the concerns about the proper initial volume for the system. The population of low-spin objects is of particular interest as potential environments that favor the formation of massive black holes, since in these systems the hydrodynamic collapse of the gas is not inhibited by the centrifugal barrier as in typical systems (e.g., typical disk galaxies are larger than their Schwarzschild radius by 6–8 orders of magnitude because of rotational support). In Paper II we show that the existence of low-spin systems at high redshifts can in principle account for the seeds of quasar black holes with masses $\gtrsim 10^6\ M_\odot$ and a comoving density of bright galaxies. Appendix A then shows that if a black hole forms in the initial collapse of a high-σ peak on the $\sim 10^8\ M_\odot$ mass scale, it is likely to be surrounded by a highly overdense region even on the mass scale of a galactic bulge. Due to the proximity of the centers of mass of the two systems, the black hole will sink by dynamical friction to the center of the bulge system after it forms. The later collapse of the surrounding region would fuel the black hole and result in the quasar activity (Loeb & Rasio 1994). In the application of the ellipsoid model to the formation of quasar progenitors, we are free to consider only the inner part of the collapse and to neglect subsequent accretion, since the formation of the black hole seed occurs on a short timescale relative to this accretion. The main remaining uncertainty in this treatment is the omission of higher multipole torque couplings.

Given a primordial power spectrum of Gaussian density perturbations, the ellipsoid model makes definite predictions about the statistics of shapes and angular momenta of overdense regions in the universe. It would first be useful to compare the quantitative predictions of our model to the statistical properties of collapsing regions in high-resolution simulations (Bertschinger 1993 and references therein). Such a comparison would require large simulated volumes ($\gtrsim$[100 Mpc]^3) in order to obtain reasonable statistical samples of rare objects that collapse today ($M \gtrsim 10^{15}\ M_\odot$). The prominence of filaments and sheets relative to quasi-spherical structures could also be tested observationally using galaxy surveys (e.g., Geller & Huchra 1989; Maddox et al. 1990; Saunders et al. 1991; Shectman et al. 1992; Strauss et al. 1992; or the future Sloan Digital Sky Survey, Gunn & Knapp 1993) to infer the smoothed mass distribution on scales larger than the virialized cores of clusters of galaxies. A nonspherical analysis of this type can provide constraints which are complementary to the conventional results obtained by applying spherical filters to galaxy surveys.

We thank John Dubinski and David Weinberg for useful discussions. D. J. E. was supported in part by a National Science Foundation Graduate Research Fellowship.

APPENDIX A

PROBABILITY DISTRIBUTION FOR THE INITIAL DATA

Our model has $6N + 5$ real numbers as its initial data, each of which is defined as some integral over the initial density field. In this Appendix we derive the probability distribution for these initial data in terms of the properties of the Gaussian random field of initial density perturbations.

We denote the radii of the boundaries between the shells as $R_0, R_1, \ldots, R_N$, where $R_N = \infty$. The values to be derived from the field are ($m = 0, \pm 1, \pm 2$):

$$\bar{\delta}(R_n) = \left(\frac{3}{4\pi R_n^3}\right)\int_{|\boldsymbol{r}|<R_n} d^3r\,\delta(\boldsymbol{r}) \qquad \text{for } n = 0, 1, \ldots, N-1\ ; \tag{A1}$$

$$q_{2m} = \rho_b \int_{|\boldsymbol{r}|<R_0} d^3r\,\delta(\boldsymbol{r}) r^2 Y^*_{2m}\ ; \tag{A2}$$

$$b^{(n)}_{2m} = \rho_b \int_{R_n<|\boldsymbol{s}|<\infty} d^3s\, Y^*_{2m}\,\delta(\boldsymbol{s}) s^{-3} \qquad \text{for } n = 0, 1, \ldots, N-1\ . \tag{A3}$$

From these values, we can easily transform back to our model input variables in equation (34) and (33), noting

$$a^{(n)}_{2m} = b^{(n-1)}_{2m} - b^{(n)}_{2m} \qquad \text{for } n = 1, 2, \ldots, N-1\ . \tag{A4}$$

Let us first switch to a multipole expansion of the Gaussian random field, as described by Binney & Quinn (1991). We replace the random field $\delta(\boldsymbol{x})$ by a new set of random functions $\{\delta_{lm}(k)\}$:

$$\delta(\boldsymbol{x}) = \sqrt{\frac{2}{\pi}} \sum_{l=0}^{\infty} \sum_{m=-l}^{l} \int_0^\infty dk\,\delta_{lm}(k) k j_l(kr) Y_{lm}(\theta, \phi)\ , \tag{A5}$$

where j_l are the spherical Bessel functions and (r, θ, ϕ) are spherical coordinates. Binney & Quinn (1991) show that the set of functions $\{\delta_{lm}\}$ is Gaussian distributed as

$$P[\{\delta_{lm}(k)\}] \propto \prod_{l,m} \exp\left[-\int_0^\infty dk\,\frac{|\delta_{lm}(k)|^2}{2P(k)}\right], \tag{A6}$$

where $P(k)$ is the power spectrum. This means that the functions $\delta_{lm}(k)$ are independent and that all of them have the same simple probability distribution.

When we insert equation (A5) into equations (A1)–(A3), the angular integrals may be easily done. The q_{2m} and $b^{(n)}_{2m}$ coefficients depend only on $\delta_{2m}(k)$, and $\bar{\delta}(R_n)$ depends only on $\delta_{00}(k)$. All the other l in the expansion do not appear, so we do not need to determine those $\delta_{lm}(k)$. Furthermore, the values we seek fall into six independent sets, since none of the integrals in equations (A1)–(A3) mix different (l, m) sets.

We next perform the radial integrals by using the identities (Abramowitz & Stegun 1965)

$$\frac{d}{dz}\left[z^{n+1} j_n(z)\right] = z^{n+1} j_{n-1}(z)\ , \qquad \frac{d}{dz}\left[z^{-n} j_n(z)\right] = -z^{-n} j_{n+1}(z)\ . \tag{A7}$$

We thus find

$$\bar{\delta}(R_n) = \frac{3}{4\pi R_n^3}\sqrt{\frac{2}{\pi}}\int_0^\infty dk \int_0^{R_n} dr\,\delta_{00}(k) r^2 k j_0(kr) = \frac{3}{4\pi R_n^3}\sqrt{\frac{2}{\pi}}\int_0^\infty dk\,k^{-2}\,\delta_{00}(k)\int_0^{kR_0} dz\,z^2 j_0(z)$$

$$= \frac{3}{4\pi R_n^3}\sqrt{\frac{2}{\pi}}\int_0^\infty dk\,k^{-2}\,\delta_{00}(k)(kR_n)^2 j_1(kR_n) = \frac{3}{\pi\sqrt{2}}\int_0^\infty dk\,\delta_{00}(k)\frac{j_1(kR_n)}{R_n}\ . \tag{A8}$$

Similarly,

$$q_{2m} = \rho_b R_0^5 \sqrt{\frac{2}{\pi}} \int_0^\infty dk\, \delta_{2m}(k) \frac{j_3(kR_0)}{R_0} \tag{A9}$$

and

$$b_{2m}^{(n)} = \rho_b \sqrt{\frac{2}{\pi}} \int_0^\infty dk\, \delta_{2m}(k) \frac{j_1(kR_n)}{R_n} . \tag{A10}$$

Each desired quantity has been written as an integral over the $\delta_{lm}(k)$, a property that will be used later in finding the relevant probability distribution.

Before developing the joint probability for the full problem, we wish to illustrate the method by working a simpler example first. We consider the average overdensities inside two different radii and ask: given a value for the overdensity inside the smaller radius, what is the distribution for that at the larger radius? Denoting the radii R_1 and R_2, we have from equation (A9)

$$\bar{\delta}_1 = \frac{3}{\pi\sqrt{2}} \int_0^\infty dk\, \delta_{00}(k) \frac{j_1(kR_1)}{R_1} , \qquad \bar{\delta}_2 = \frac{3}{\pi\sqrt{2}} \int_0^\infty dk\, \delta_{00}(k) \frac{j_1(kR_2)}{R_2} . \tag{A11}$$

Because the functions $\delta_{lm}(k)$ are independent and because we need only consider one at a time, we will suppress the lm label. The form of the integral in equation (A6) prompts us to consider $\delta(k)$ as a vector in a function space and to define the inner product as

$$\langle a \,|\, b \rangle = \int_0^\infty \frac{dk}{P(k)} a^*(k) b(k) , \tag{A12}$$

for two arbitrary functions a and b. Next, define

$$Q_1(k) = \frac{j_1(kR_1)}{R_1} P(k) , \qquad Q_2(k) = \frac{j_1(kR_2)}{R_2} P(k) . \tag{A13}$$

Then we have

$$\bar{\delta}_1 = \frac{3}{\pi\sqrt{2}} \langle Q_1 \,|\, \delta_{00} \rangle \tag{A14}$$

and similarly for $\bar{\delta}_2$; note that the $P(k)$ in the definition of Q cancels the $P(k)$ in the inner product.

Now let us consider some basis $n_j(k)$ that is orthonormal under our inner product. Then we may write $\delta(k)$ as a linear combination of these basis vectors,

$$\delta(k) = \sum_j \beta_j n_j(k) . \tag{A15}$$

Substituting this form into equation (A6), we find the probability for a given set of β_j to occur,

$$P(\beta) \propto \exp\left(-\frac{1}{2} \sum_{i,j} \beta_i^* \beta_j \langle n_i \,|\, n_j \rangle \right) = \exp\left(-\frac{1}{2} \sum_j |\beta_j|^2 \right) = \prod_j \exp\left(-\frac{1}{2} |\beta_j|^2 \right) . \tag{A16}$$

This means that each β is independently distributed with a uniformly distributed phase and a Gaussian distributed magnitude. For an $m = 0$ function as we have here, β is real and is simply a Gaussian deviate, namely it is drawn from a Gaussian distribution with a zero mean and a unit variance.

We would like to express Q_1 and Q_2 in terms of this orthonormal basis. Since we have not yet constructed the basis, we choose it to be simple. The first vector n_1 will be Q_1 normalized,

$$n_1 = \frac{Q_1}{\sqrt{\langle Q_1 \,|\, Q_1 \rangle}} . \tag{A17}$$

Then, we pick n_2 to be the normalized component of Q_2 orthogonal to n_1, which is

$$n_2 = \frac{Q_2 - \langle n_1 \,|\, Q_2 \rangle n_1}{\sqrt{\langle Q_2 \,|\, Q_2 \rangle - \langle n_1 \,|\, Q_2 \rangle^2}} . \tag{A18}$$

We may then complete the basis any way we wish; none of the other vectors will include any component of Q_1 or Q_2. Inverting equations (A17) and (A18), we find

$$Q_1 = \sqrt{\langle Q_1 \,|\, Q_1 \rangle} n_1 , \qquad Q_2 = \langle n_1 \,|\, Q_2 \rangle n_1 + \sqrt{\langle Q_2 \,|\, Q_2 \rangle - \langle n_1 \,|\, Q_2 \rangle^2} n_2 . \tag{A19}$$

Putting equations (A9) and (A15) into equation (A14) and using the orthonormality of the basis, we find

$$\bar{\delta}_1 = \frac{3}{\pi\sqrt{2}}\sqrt{\langle Q_1|Q_1\rangle}\beta_1 \tag{A20}$$

and

$$\bar{\delta}_2 = \frac{3}{\pi\sqrt{2}}(\langle n_1|Q_2\rangle\beta_1 + \sqrt{\langle Q_2|Q_2\rangle - \langle n_1|Q_2\rangle^2}\beta_2) = \frac{3}{\pi\sqrt{2}}\sqrt{\langle Q_2|Q_2\rangle}(\gamma\beta_1 + \sqrt{1-\gamma^2}\beta_2)\,, \tag{A21}$$

where γ is the dimensionless overlap defined as

$$\gamma = \frac{\langle Q_1|Q_2\rangle^2}{\sqrt{\langle Q_1|Q_1\rangle\langle Q_2|Q_2\rangle}}\,. \tag{A22}$$

To determine $\bar{\delta}_1$ and $\bar{\delta}_2$ randomly, we simply find two Gaussian deviates β_1 and β_2 and combine them as indicated. Alternatively, if we are given $\bar{\delta}_1$ and asked to determine $\bar{\delta}_2$ given this constraint, we fix the value of β_1 to produce $\bar{\delta}_1$. Despite this constraint, β_2 remains a Gaussian deviate since it is independent of β_1, and so we may take a random value of β_2 along with our fixed value of β_1 to find the constrained distribution of $\bar{\delta}_2$.

Equation (A20) can be expanded to give

$$(\bar{\delta}_1)^2 = \frac{1}{2\pi^2}\int_0^\infty dk\,P(k)\left[\frac{3j_1(kR_1)}{R_1}\right]^2\beta_1^2\,, \tag{A23}$$

the expectation value of which is the standard expression for $\langle(\delta M/M)^2\rangle$ for a spherical top-hat window function of radius R_1 (cf. eq. [36]). Denoting this expectation value as $(\sigma_1)^2$ and similarly for $(\sigma_2)^2$, we find $\nu_1 \equiv \bar{\delta}_1/\sigma_1 = \beta_1$ and $\nu_2 \equiv \bar{\delta}_2/\sigma_2 = \gamma\beta_1 + \sqrt{1-\gamma^2}\beta_2$, so a high-$\sigma$ peak on one mass scale will correspond to a high-σ peak on the other mass scale if γ is close to 1.

For the $\Omega = 1$ CDM model amd mass scales of $10^8\,M_\odot$ and $10^{10}\,M_\odot$, we calculate $\gamma \approx 0.74$. This means, for example, that given a 3 σ peak at $10^8\,M_\odot$, the surrounding $10^{10}\,M_\odot$ region has an overdensity of $\nu_2 = 2.22 \pm 0.67\beta$, where β is a Gaussian deviate. This result has interesting physical implications to the problem of the origin of quasar black holes discussed in Paper II. If a black hole forms in the initial collapse of a high-σ peak on the $\sim 10^8\,M_\odot$ mass scale, it is likely to be surrounded by a highly overdense region even on the mass scale of a galactic bulge.

We now need to generalize the above method to an arbitrary number of vectors. We seek p values from the field, denoted $f_1, f_2, \ldots, f_p$, and each may be written as some integral over a particular $\delta_{lm}(k)$; only one (l, m) is involved and so we suppress the index here as well. Then, we define the $Q_j(k)$ by the relations

$$f_j = \int_0^\infty \frac{dk}{P(k)}\,\delta(k)Q_j(k)\,, \tag{A24}$$

where all of the Q_j are real-valued functions; and define the matrix M,

$$M_{ij} = \langle Q_i|Q_j\rangle = \int_0^\infty \frac{dk}{P(k)}\,Q_i(k)Q_j(k)\,. \tag{A25}$$

We now seek an orthonormal basis $\{n_j\}$ with the property that

$$Q_i = \sum_{j=1}^{p} L_{ij}n_j\,, \tag{A26}$$

where L is a lower triangular matrix and the remaining n_j are not used. Substituting equation (A26) into equation (A25) and using the orthonormality property, we find

$$M_{ij} = \sum_p L_{ip}L_{jp}\,. \tag{A27}$$

Hence, our basis must be defined by $M = LL^T$. Can we find such an L? In fact we can, for if M is positive-definite symmetric matrix, this is the Cholesky decomposition (Press et al. 1992, § 2.9). M is obviously symmetric and must be positive-definite if $P(k) > 0$ for all k, and so we may find a unique L.

Next, we take $\{n_j\}$ as the basis for $\delta(k)$. Then, as before, we decompose by equation (A15) and reach the probability distribution in equation (A16). Substituting this result, as well as equation (A26), into equation (A24), we get

$$f_j = \int_0^\infty \frac{dk}{P(k)}\sum_{p,q}\beta_p n_p L_{jq}n_q = \sum_p L_{jp}\beta_p\,. \tag{A28}$$

This completes the solution. One needs only to specify p Gaussian deviates and combine them in the indicated way in order to get realizations of the p values f_j. To construct the L matrix, one must perform $p(p+1)/2$ one-dimensional integrals as given in equation (A25). This task can be made even simpler by doing the integrals together since they have many functional evaluations in common.

In the particular case of the initial conditions for the ellipsoid model, we have six sets of parameters to determine, one for $l = 0$ and five for $l = 2$. But the five $l = 2$ sets are equivalent and will share one L matrix. Also, the integral forms for $l = 0$ in equation (A8)

are identical to those for $l = 2$ as given in equation (A11). The only difference between the two sets is the one additional initial condition presented in equation (A9). In order to compute L for the $l = 0$ set, we need not calculate any new integrals; we simply take the required integrals as a submatrix of M from the $l = 2$ calculation and compute a new Cholesky decomposition.

Because the original field $\delta(x)$ was real, the complex functions $\delta_{lm}(k)$ have the usual spherical harmonic relation between them, i.e., $\delta_{lm}(k) = (-1)^m \delta^*_{l-m}(k)$. Thus, for $m \neq 0$ there are four real functions: the real and imaginary parts of $\delta_{lm}(k)$ and $\delta_{l-m}(k)$, only two of which are independent. Returning to equations (14) and (20), where $l = 2$, we choose to work with the real and imaginary parts of $m = 1$ and $m = 2$ as well as the real term $m = 0$ as the five independent real parameters. This means that instead of asking for q_{2m} and $b^{(n)}_{2m}$ as in equations (A2) and (A3), we compute Re q_{22}, Im q_{22}, Re q_{21}, Im q_{21}, and q_{20}, and the same for $b^{(n)}$. This is easy to do by simply taking the quantities Re $\delta_{22}(k)$, Im δ_{22}, ..., as the independent random functions. The $l = 2$ values again fall into five independent sets, each being treated as above. There is, however, one modification, as seen from the original multipole field probability distribution in equation (A6):

$$P[\delta(x)] \propto \exp\left[-\sum_{l,m}\int_0^\infty dk\,\frac{|\delta_{lm}|^2}{2P(k)}\right] = \exp\left[-\sum_l \int_0^\infty dk\,\frac{2(\text{Re }\delta_{ll})^2 + 2(\text{Im }\delta_{ll})^2 + 2(\text{Re }\delta_{l(l-1)})^2 + \cdots + (\delta_{l0})^2}{2P(k)}\right]. \quad \text{(A29)}$$

This indicates that the real and imaginary parts of the $m \neq 0$ terms actually are distributed with half the variance of the $m = 0$ term. The simplest way to incorporate this fact is to compute all the $l = 2$ sets as for the $m = 0$ case and then take the β_j to have variance of one-half rather than unity for $m \neq 0$.

Finally, there is a choice as to what order to place our f_j in the vector. Since the matrix L is a lower triangular, the value f_1 requires only one Gaussian deviate to be determined. As discussed in § 4, there are additional constraints that we place on the initial conditions. Since these are imposed simply by rejecting any set of initial data that do not satisfy them, it is most efficient to pick the most discriminating test to be f_1. In particular, the test that $\delta(R_0) > \nu_{\min}\sigma$ is very stringent and we arrange the $l = 0$ functions so that this condition is the first basis function. This way, we need only find one Gaussian deviate before applying this test.

APPENDIX B

TREATMENT OF AN AXIS COLLAPSE

The inclusion of a collapsed axis is complicated by the facts that the ellipsoid is rotating and that the columns of the matrix A need not be orthogonal. When we halt the collapse of an axis, we wish only to end the radial collapse and to leave the tangential velocity unchanged.

First, we must identify that an axis has reached 40% of its turnaround value. At each time step, we diagonalize $AA^T = Q\Lambda Q^T$ to find the axis lengths, which are in $\sqrt{\Lambda}$. We put these in ascending order and compare each to the previous maximum length for the short, middle, and long axes. If the new length is longer, we save it as the new maximum. If the new length is less than 40% of the maximum for that axis, we assume that the axis has collapsed and save the column number so as to be able to refer to it in Q and Λ. This method of identifying the axes by sorting the lengths works well because the axes are well-separated soon after the beginning of the integration and well before turnaround.

If a particular axis has collapsed, we remove the radial component of the velocity in that direction and we alter the right-hand side of the equation of motion (8) so that there is no inward force in that direction. The steps for each alteration are equivalent, so we only describe the first in detail.

Suppose we begin from the diagonalization $AA^T = Q\Lambda Q^T$ and want to fix the αth axis. The position of mass elements within the ellipsoid may be written as $\boldsymbol{r} = Q\sqrt{\Lambda}\boldsymbol{s}$, where $\boldsymbol{s}$ is a vector on the unit sphere. Then the frozen axis is $\boldsymbol{s} \parallel \boldsymbol{e}_\alpha$, the Cartesian basis vector. The velocity field is $\boldsymbol{v} = \dot{A}A^{-1}Q\sqrt{\Lambda}\boldsymbol{s}$, where $\dot{A} = dA/dt$. We now rotate this velocity to the principal axis frame of the ellipsoid, which requires left-multiplying by Q^T. This is obtained by defining

$$\tilde{V} = Q^T\dot{A}A^{-1}Q\sqrt{\Lambda}\,, \quad \text{(B1)}$$

where $\tilde{V}_{jk}$ is the jth component of the velocity at the point in the direction of the kth axis, and the axes are numbered according to the columns of Q.

Now we can remove the αth component of velocity along the αth axis by removing the $\alpha\alpha$ component of $\tilde{V}$. We therefore define a new matrix W such that

$$U_{\beta\gamma} = \begin{cases} 0, & \text{if } \beta = \alpha \text{ and } \gamma = \alpha\,, \\ \tilde{V}_{\beta\gamma}, & \text{otherwise}\,. \end{cases} \quad \text{(B2)}$$

Then we need to connect this matrix back to the new velocity matrix $\dot{A}_{\text{new}}$. We do this by solving equation (B1) for $\dot{A}$ after replacing $\tilde{V}$ by U. Then we replace the old matrix for $\dot{A}$ with

$$\dot{A}_{\text{new}} = QU\sqrt{\Lambda}^{-1}Q^TA\,. \quad \text{(B3)}$$

If more than one axis has collapsed, we modify the definition of U to eliminate all diagonal elements corresponding to the collapsed axes. This algorithm works equally well for the forces by substituting $\ddot{A} \equiv d^2A/dt^2$ for $\dot{A}$ everywhere. Since this procedure does not modify the tangential velocities, it preserves angular momentum; however, it does change the vorticity.

APPENDIX C

RELATION BETWEEN SHEAR AND OVERDENSITY

In this Appendix we present a calculation separate from the dynamical ellipsoid model, but yet based upon the formalism discussed in this paper. As before, we begin by dividing the universe into two pieces through a spherical boundary of radius R around the origin. We now wish to compare the statistical properties of the average overdensity in the interior region $\bar{\delta}(R)$ (cf. eq. [15]) to those of the quadrupole shear resulting from the exterior region a_{2m} (cf. eq. [2]). We will show that these quantities are drawn from independent Gaussian distributions whose variances are related by a constant of proportionality that is independent of the power spectrum or mass scale.

From equations (A1), (A3), (A8), and (A11), we can easily relate $\bar{\delta}$ and a_{2m} to integrals over the coefficients of the multipole expansion of the Gaussian random field:

$$\bar{\delta} = \frac{3}{\pi\sqrt{2}} \int_0^\infty dk\, \delta_{00}(k) \frac{j_1(kR)}{R}, \tag{C1}$$

and

$$a_{2m} = \rho_b \sqrt{\frac{2}{\pi}} \int_0^\infty dk\, \delta_{2m}(k) \frac{j_1(kR)}{R}. \tag{C2}$$

Because each of these six quantities depends upon different δ_{lm}, they will be independent. By the methods of Appendix A, we find that the six quantities are Gaussian distributed with a zero mean and the variances

$$\langle \bar{\delta}^2 \rangle = \left(\frac{3}{\pi\sqrt{2}}\right)^2 \int dk\, P(k) \left[\frac{j_1(kR)}{R}\right]^2, \tag{C3}$$

$$\langle (a_{20})^2 \rangle = \left(\rho_b \sqrt{\frac{2}{\pi}}\right)^2 \int dk\, P(k) \left[\frac{j_1(kR)}{R}\right]^2, \tag{C4}$$

and

$$\langle (\mathrm{Re}\ a_{22})^2 \rangle = \langle (\mathrm{Im}\ a_{22})^2 \rangle = \langle (\mathrm{Re}\ a_{21})^2 \rangle = \langle (\mathrm{Im}\ a_{21})^2 \rangle = \frac{1}{2} \langle (a_{20})^2 \rangle. \tag{C5}$$

The last equation follows from equation (A29) and the discussion around it.

The key result of this derivation is that the integrals in equations (C3) and (C4) are identical. We can therefore pull all of the dependence on the power spectrum into one constant. We define σ as the rms amplitude of $\delta M/M$ according to equation (36). We may then write $\bar{\delta} = \sigma\nu$, $a_{20} = (2\sqrt{\pi\rho_b/3})\sigma z_1$, Re $a_{22} = (\sqrt{2\pi\rho_b/3})\sigma z_2$, Im $a_{22} = (\sqrt{2\pi\rho_b/3})\sigma z_3$, Re $a_{21} = (\sqrt{2\pi\rho_b/3})\sigma z_4$, and Im $a_{21} = (\sqrt{2\pi\rho_b/3})\sigma z_5$, where ν and the $\{z_j\}$ are all Gaussian deviates of unit variance.

We next consider how the inner region would evolve given these values as the initial conditions. In particular, we apply the Zel'dovich approximation to find whether all the material of the interior region will turn around and form a spatially bounded object or whether the region will expand forever in at least one direction. For an $\Omega = 1$ universe and under the Zel'dovich approximation, this question is simply a matter of whether the initial peculiar velocities have inward radial components or not. This, in turn, depends on the initial gravitational potential (as we assume growing mode velocities), which we may construct from equations (12) and (14) to get the matrix

$$\Phi_{\alpha\beta} = \frac{4\pi G\rho_b \sigma}{3} (\nu I_{\alpha\beta} + S_{\alpha\beta}), \tag{C6}$$

where I is the identity matrix and

$$S = \sqrt{\frac{3}{5}} \begin{pmatrix} z_2 - \frac{z_1}{\sqrt{3}} & z_3 & z_4 \\ z_3 & -z_2 - \frac{z_1}{\sqrt{3}} & z_5 \\ z_4 & z_5 & \frac{2z_1}{\sqrt{3}} \end{pmatrix}. \tag{C7}$$

We want Φ to have positive eigenvalues, which means that the eigenvalues of S must be greater than $-\nu$. The probability that a spherical region of overdensity ν will expand without bound in one direction due to shear depends only on the distribution of the random matrix S. All reference to the power spectrum has been removed.

Table 1 shows the cumulative distribution function for the most negative eigenvalue $-\mu$ ($\mu > 0$) of the matrix S. This quantity acts as a negative ν, counteracting the actual $\nu = \bar{\delta}/\sigma$ that one normally identifies as the parameter controlling gravitational collapse.

TABLE 1

PROBABILITY THAT MOST NEGATIVE EIGENVALUE $-\mu$ OF S IS GREATER THAN THRESHOLD $-\mu_0$

μ_0	$P(\mu < \mu_0)$
0.20	0.01%
0.31	0.1
0.53	1
0.91	10
1.19	25
1.55	50
1.96	75
2.36	90
3.11	99
3.69	99.9

The importance of shear through the collapse is evident from the prevalence of large values of μ. For low Ω universes, one might alter the peculiar velocity requirement as discussed in § 4 (cf. eq. [35]); this leads to the requirement that $\nu - \mu > \bar{\delta}_{\rm crit}/\sigma$.

The above calculation provides insight to the acceptance rate for the velocity constraint that we use in the ellipsoid model. In this model, there is an additional term in the potential coming from the anisotropy of the ellipsoid. This term tends to slightly increase the acceptance (i.e., resist the shear) because the long axis of the ellipsoid tends to be aligned with the most negative shear axis. The above calculation also has implications to the Press-Schechter formalism (Press & Schechter 1974), in which spherical regions with a sufficiently high ν are all assumed to turn into objects at the appropriate collapse time. However, as it stands the model can eliminate objects only on the basis of shear, some of which would presumably be reintroduced through mergers of lower mass systems or fragmentation of unbound filaments.

REFERENCES

Abell, G. O. 1958, ApJS, 8, 211
Abramowitz, M., & Stegun, I. A. 1965, Handbook of Mathematical Functions (New York: Dover)
Bardeen, J. M., Bond, J. R., Kaiser, N., & Szalay, A. S. 1986, ApJ, 304, 15
Barnes, J., & Efstathiou, G. 1987, ApJ, 319, 575
Bertschinger, E. 1993, Physica D, submitted
Bertschinger, E., & Gelb, J. M. 1991, Comp. Phys., 5, 164
Bertschinger, E., & Jain, B. 1994, ApJ, in press
Binney, J., & Quinn, T. 1991, MNRAS, 249, 678
Binney, J., & Tremaine, S. 1987, Galactic Dynamics (Princeton: Princeton Univ. Press)
Birkinshaw, M., & Hughes, J. P. 1994, ApJ, 420, 33
Bond, J. R., & Myers, S. T. 1994, ApJ, submitted
Carlson, B. C. 1977, SIAM J. Math. Anal., 8, 231
Cen, R., & Ostriker, J. P. 1993, ApJ, 417, 415
Doroshkevich, A. G. 1970, Astrofizika, 6, 581
Dubinski, J. 1992, ApJ, 401, 441
Eisenstein, D. J., & Loeb, A. 1995, ApJ, in press (Paper II)
Efstathiou, G., & Jones, B. J. T. 1979, MNRAS, 186, 133
Fukugita, M., Okamura, S., & Yasuda, N. 1993, ApJ, 412, L13
Geller, M. J., & Huchra, J. P. 1989, Science, 246, 897
Gunn, J. E., & Gott, J. R. 1972, ApJ, 176, 1
Gunn, J. E., & Knapp, G. R. 1993, in Sky Surveys: Protostars to Protogalaxies, ed. B. T. Soifer (ASP Conf. Proc. 43), 267
Hoffman, Y. 1986a, ApJ, 301, 65
———. 1986b, ApJ, 308, 493
———. 1988, ApJ, 329, 8
Hoyle, F. 1949, in Problems of Cosmical Aerodynamics, ed. J. M. Burgers & H. C. van de Hulst (Dayton: Central Air Documents Office), 195
Icke, V. 1973, A&A, 27, 1
Lin, C. C., Mestel, L., & Shu, F. H. 1965, ApJ, 142, 1431
Lynden-Bell, D. 1964, ApJ, 139, 1195
Loeb, A., & Rasio, F. A. 1994, ApJ, 432, 52
Maddox, S. J., Efstathiou, G., Sutherland, W. J., & Loveday, J. 1990, MNRAS, 242, 43P
McHardy, I. M., Stewart, G. C., Edge, A. C., Cooke, B. A., Yamashita, K., & Hatsukade, I. 1990, MNRAS, 242, 215
Merritt, D., & Hernquist, L. 1991, ApJ, 376, 439
Park, C. 1990, MNRAS, 242, 59P
Peebles, P. J. E. 1969, ApJ, 155, 393
———. 1980, The Large Scale Structure of the Universe (Princeton: Princeton Univ. Press)
———. 1993, Principles of Physical Cosmology (Princeton: Princeton Univ. Press)
Press, W. H., & Schechter, P. 1974, ApJ, 187, 425
Press, W. H., Teukolsky, S. A., Vetterling, W. T., & Flannery, B. P. 1992, Numerical Recipes in C (2d ed.; Cambridge: Cambridge Univ. Press)
Quinn, T., & Binney, J. 1992, MNRAS, 255, 729
Ryden, B. S. 1988, ApJ, 329, 589
Saunders, W., et al. 1991, Nature, 349, 32
Shandarin, S. F., & Zel'dovich, Ya. B. 1989, Rev. Mod. Phys., 61, 185
Shectman, S. A., Schechter, P. L., Oemler, A. A., Tucker, D., Kirshner, R. P., & Lin, H. 1992, in Clusters and Superclusters of Galaxies, ed. A. C. Fabian (Dordrecht: Kluwer)
Strauss, M. A., Davis, M., Yahil, A., & Huchra, J. P. 1992, ApJ, 385, 421
van de Weygaert, R., & Babul, A. 1994, ApJ, 425, L59
Warren, M. S., Quinn, P. J., Salmon, J. K., & Zurek, W. H. 1992, ApJ, 399, 405
White, S. D. M. 1984, ApJ, 286, 38
———. 1993, private communication
White, S. D. M., & Silk, J. 1979, ApJ, 231, 1
Zel'dovich, Ya. B. 1965, Soviet Astron.-AJ, 8, 700
———. 1970, A&A, 5, 84